HIPERWIND

HIghly advanced Probabilistic design and Enhanced Reliability methods for high-value, cost-efficient offshore WIND

Title: Environmental joint probability distributions and uncertainties
Deliverable no: D2.3

Delivery date: 31.01.2022
Lead beneficiary: DTU
Dissemination level: Public

This project has received funding from the European Union's Horizon 2020 Research and Innovation Programme under Grant Agreement No. 101006689

Author(s) information (alphabetical):

Name	Organisation	Email
Mark Kelly	DTU	MKEL@dtu.dk
Eric Vanem	DNV	Erik.Vanem@dnv.com

Acknowledgements/Contributions:

Name	Organisation	Email

Document information:

Version	Date	Description	Prepared by	Reviewed by	Approved by
1	31 Jan. 2022	Main report	Mark Kelly	Nikolay Dimitrov	Karen Hyllested Thielsen
2	1 Feb. 2022	Edited & added DNV part on wind-wave PDFs	Mark Kelly & Erik Vanem	Nikolay Dimitrov	Karen Hyllested Thielsen

Definitions:

Contents

List of Abbreviations

ABL	Atmospheric Boundary Layer
DLC	Design Load Case(s) from IEC 61400-1 standard
DNV	Den Norske Veritas (partner in Hiperwind)
DTU	Danish Technical University
D2.3	Deliverable 2.3 of HiperWind
GEV	Generalized Extreme Value (probability distribution type)
GPD	Generalized Pareto Distribution
jPDF	joint Probability Density Function
OWA	Offshore Wind Accelerator 2019 project on ramps and windfarm loads
PDF	Probability Density Function
UiB	University of Bergen (“*Universitet i Bergen*”)
WP	Work Package

1. Executive Summary

Extreme events and their underlying mechanisms are investigated through novel blended approaches, based on measured datasets. This report documents in detail the relevant site-specific joint probability distributions [jPDF] for such events, driven by inputs from tasks 2.1–2.4 (dealing with atmospheric characterization and modelling) and datasets from WP1 (data acquisition).

The spectral characteristics, severity, and frequency of occurrence of transient high-amplitude events are described and their statistics are given, for use in other WP of the project. An innovative method is developed to identify all load-driving events, regardless of their generating mechanisms or specific signature; extreme events of different character are indeed found (e.g. wind ramps, entrainment effects, frontal passages, breaking wave-turbulence), per characteristic turbine response time (effective filter frequency). We include relevant joint probability distributions for such events, and have also provided timeseries to project partners for the extreme events. A new method for technique for obtaining Mann-model turbulence parameters is also created, and used to find these parameters corresponding to the identified extremes and their timeseries; the parameters are also provided to partners within Hiperwind.

2. Introduction

In work package 2 (WP2) of Hiperwind we are focused on representation and modelling of environmental conditions, namely wind and waves. The outputs from WP2 primarily feed WP3, which entails loads modelling for wind turbines and windfarms; it and WP3 together also drive WP4 and WP5, which involve life assessment of turbine structures and components respectively.

This deliverable (D2.3) is concerned with statistical characterization of load-driving wind events relevant for the design and operation of offshore wind turbines and wind farms, as well as the combined air-sea conditions. This includes the joint probability distributions of appropriate variables, which describe the severity and rate of occurrence of such events as well as identifying the events. Also included in D2.3 are the spectral characteristics associated with the various load-driving events, along with the spectral description of the background flow within which these events are embedded.

In addition to the joint distributions of relevant flow (wind) field variables which are the focus of this report, in WP2 we additionally consider the joint statistical behavior of the wind and relevant sea-state variables, i.e., so-called ‘met-ocean’ distributions; these especially add information for the design of floating turbines. Due to confidentiality issues and proprietary information from the TeeSide wind farm, much of the latter analysis is not reported here, but distributed within the project as data; the wind statistics also include output (e.g. filtered timeseries and statistics) which are shared as data within Hiperwind.

3. Investigation of load-driving wind events

3.1. Background

In common industrial practice and the corresponding IEC 61400-1 standard for wind turbine design, load-driving conditions have generally been simulated using simplified scenarios that are considered representative of the most critical parts of the design load envelopes. The magnitude of the wind events in these scenarios is characterized (‘guessed’) based on 10-minute statistics, i.e. via the standard deviation of wind speed. A developing trend has been to consider the matching of observed phenomena to individual design-load cases [DLCs] within the 61400-1, with Nielsen *et al.* (2004) giving a first basis for statistical characterization efforts and constrained turbulence simulation. Nielsen *et al.* (2004) looked at examples of gusts and occurrence rates of wind speed jumps, recognizing the need for filtering, but their analysis was essentially limited to the surface-layer regime (10m heights) where large accelerations inextricably intertwined with ground-affected turbulence.[1] Works such as Hansen & Larsen (2007) made early comparisons of measurements to extreme-event DLC’s, though from limited data; Larsen & Hansen (2008) offered calibration of the IEC DLC’s, though they assumed extreme events to be turbulence-driven and connected with 10-minute statistics per the IEC. Later, wind speed ramp events were detected directly at heights of contemporary turbines ($z \geq 100$m), and their statistics compared to the

---

[1] Nielsen *et al.* (2004) also identified some nonstationary wind and direction timeseries from a limited dataset, which they attributed to frontal passages, and which did not appear to give large accelerations compared to the DLC’s associated with wind direction changes in IEC 61400-1 standard. However, these were qualitative, affected by the limited amount of data, and superseded by later work such as Hannesdóttir *et al.* (2019).

IEC's coherent gust with direction change [ECD] design-load case (Hannesdóttir & Kelly, 2019), showing that direction changes due to such events may exceed the IEC prescription but with a broad range of rise times and magnitudes. Hannesdóttir *et al*. (2019) found these events to not exceed the IEC's extreme turbulence prescription, with the exception of some events crossing rated speed for a turbine, which gave tower-base fore-aft loads exceeding DLC1.3 of the 61400-1. The ramp-associated accelerations, rather than their amplitudes, appeared to be driving the excessive loads; this was confirmed in the 2019 Offshore Wind Accelerator [OWA] windfarm-ramp study of Kelly *et al.* (2021). Finding the climatological (long-term) joint-PDF of bulk acceleration, post-ramp speed, and upper-rotor shear for wind ramp events, Kelly *et al.* (2021) used this jPDF to synthesize an ensemble of representative coupled flow/aeroelastic simulations for an offshore wind farm[2]; they found that ramp-associated accelerations crossing rated speed drove the largest thrust-based turbine loads, and that most wind speed ramps were quite large[3] and persist through the wind farm.

3.2. Data and Methodology

As written above, wind *accelerations* have been seen to most impact loads in operating conditions, and that 'fast' data (sampled at a rate of at least 1 Hz) is needed to capture such. Considering this, and that mechanisms other than wind ramps—including turbulence—can cause peak loads on operating turbines, we have chosen a more general and robust methodology, compared to attempting to detect events corresponding to specific physical mechanisms. Namely, toward a universal description, we build a statistical characterization of the wind accelerations at the heights impacting offshore wind turbines. This is done by using 15.4 years (Oct.2004–Mar.2020) of high-frequency observations (10–20 Hz) from the Høvsøre turbine test station, located on the west coast of Denmark (Peña *et al.*, 2019). In particular, we select data where the wind originates from offshore (the dominant and most common wind directions). One mast was primarily used, with 10 Hz speed and direction data from heights of 100m and 160m; lower sensors at 60m and 10m were not used, due to their measurements being affected by the coastline. A secondary mast 400m to the south (same distance from the N-S coastline) was also used in a supplementary way, exploiting its sonic anemometers at 80m and 100m to test three-component turbulence calculations; this is described later. To start we are interested in load-driving events without joint occurrence of irregular turbine conditions, i.e. away from cut-in and cut-out; thus we select data under the conditions $(8\,\mathrm{m/s} + \sigma_u) \leq U \leq (18\,\mathrm{m/s} - \sigma_u)$, along with $\sigma_u > 0.3$ m/s and the aforementioned offshore directional criterion (conservatively 240°–300°). This is chosen for practicality: previous studies found the loads induced by ramp accelerations tended to be largest around rated speed, which tends to be 12–13 m/s; further, due to sample rates of 10–20 Hz, and calculating many quantities including numerous Fourier spectra, we must limit the number of samples processed due to computational constraints.

Nielsen *et al*. (2004) and others have noted that to examine statistics in wind speed jumps, one needs to filter the wind timeseries. However, in our study here we note that there are some additional details that

---

[2] The coupled simulations (model-chain) involved constrained turbulence simulations coupled to both aeroelastic model, as well as driving large-eddy simulations coupled to aeroelastic models.

[3] Most ramp events have rise-times of tens to hundreds of seconds, presumably due mostly to frontal passages. These and the simulated events in Kelly *et al.* (2021) correspond to scales of ~0.5–10 km.

allow analysis of load-driving accelerations. First, one must take care with calculating accelerations from timeseries: simple finite-differences do not suffice, as they can especially impact the acceleration maxima in unpredictable ways due to their oscillatory spectral signature. Accelerations must be calculated in Fourier space, exploiting $\dot{u} \equiv du/dt = \mathcal{F}^{-1}[f^2 S_{uu}(f)]$, where $\mathcal{F}^{-1}$ denotes the inverse Fourier transform, S_{uu} is the power spectrum of u, and f denotes temporal frequency in Hz. An example of acceleration spectra is given in Figure 1, using different ways to calculate the acceleration, and also showing the spectra with a low-pass filter having filter-frequency $f_c = 0.1$ Hz. In the figure one can see that using $\Delta s/\Delta t$ to approximate ds/dt causes significant inflation of fluctuations at smaller scales and suppression of larger-scale (low-*f*) fluctuations. The green and red lines in the plot show these, i.e. low-pass filtered spectra of explicit first-order finite difference, and alternately using Mathematica's `differentiator filter` with Blackman-Nuttall window, respectively. We also remind that using the implicit low-pass filtering due to finite-differencing is not as easily nor precisely controlled, compared to explicitly applying a filter; here (and in Figure 1) we use a second-order Butterworth filter (black line).

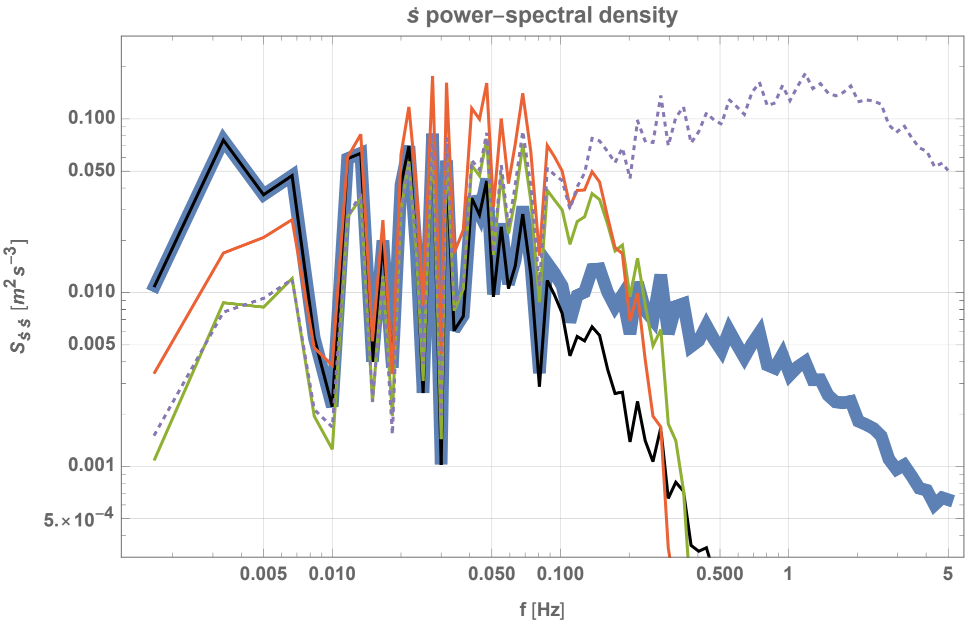

Figure 1. Spectrum of accelerations from a 10-minute timeseries of wind speed sampled at 10Hz, calculated in different ways: smoothed spectrum of $f^2S_{ss}(f)$, i.e. spectral definition of ds/dt (thick blue); 2nd-order Butterworth filtered ds/dt (black); Δs/Δt (dotted); digitally low-pass filtered Δs/Δt (green); digital differentiator filter (red). Filter cutoff is f_c=0.1 Hz, and smoothing of 30 points/decade is done to cleanly display the effects.

The dotted line in Figure 1 also reminds of the *need* for low-pass filtering of acceleration spectra, as well as problems that finite-difference approximation causes: we must filter high-frequency timeseries using a filter appropriate for the characteristic response of wind turbines, to avoid counting small-scale noise that does not appreciably impact turbines; but we must also avoid finite-difference (non-spectral) calculation of accelerations, to avoid inflation of such noise (also evidenced by green and red lines in figure).

To allow for different turbine response times, we calculate statistics for three different low-pass filter scales, i.e. f_c^{-1} ={30s, 10s, 3s}. A second-order Butterworth filter is used, though we also include some comparisons below involving sixth-order Butterworth.

In addition to Fourier-based calculation of filtered accelerations, in order to build meaningful statistics for load-driving events we consider the top 1% of accelerations per each 10-minute period. In other words, we calculate P_{99} of the filtered $\dot{s}$ using the CDF of $\dot{s}$ for every 10-minute record; from the collections of such $\dot{s}_{99}$ (for different response times) we can calculate long-term statistics. This method is preferable to using 10-minute maxima of accelerations, because the latter do not necessarily correspond to some probability per 10 minutes; conversely, P_{99} is relatable via probability distributions, and more independently of record size.

3.3. Analysis

To demonstrate/visualize the methodology and statistics that we are building from—as described in the paragraphs just above, Figure 2 shows how the maximum, 99th percentile, and 90th percentile of low-pass filtered streamwise accelerations vary with filter frequency (response time); this is done for two different 10-minute periods of wind speeds, measured at 160m height. In the figure we show a 'typical' period corresponding to oft-observed 10-minute acceleration maxima, as well as a plot for a 10-minute period corresponding to one of the top 10 long-term maxima of 10-minute $P_{99}(ds/dt)$.

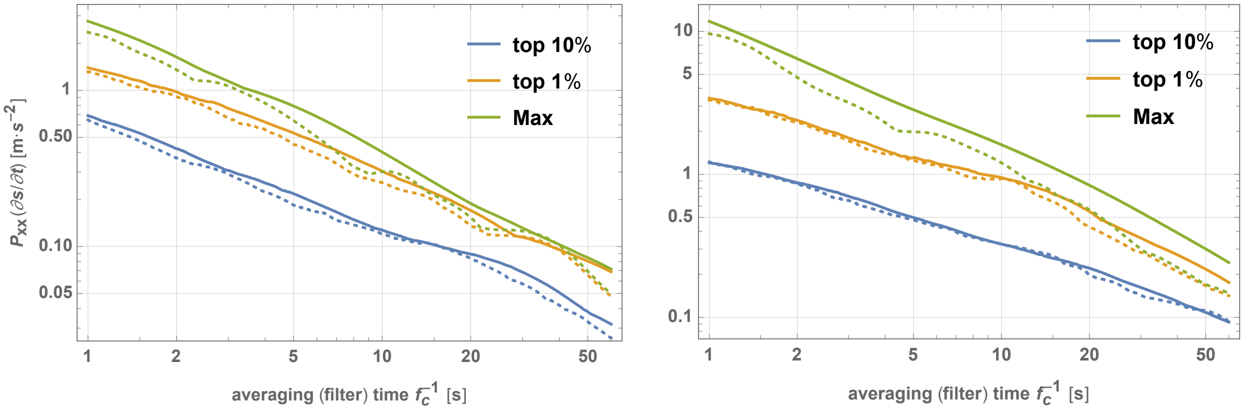

Figure 2. Dependences of 90th percentile, 99th percentile, and maximum of filtered acceleration, vs. filter frequency (response time) using O2 Butterworth low-pass filter. Two different 10-minute periods shown, for wind speeds recorded at 160m height. Left: typical/commonly-occurring record; right: a case of load-driving accelerations (a long-term maximum per wind speed bin). Solid and dotted lines indicate 2nd and 6th order low-pass Butterworth filtered accelerations, respectively.

In Figure 2 we see that the filter order has a relatively small effect, particularly for the 99th and 90th percentile, compared to its effect on the 10-minute maximum of filtered acceleration; this shows some justification for use of $P_{99}(ds/dt)$ instead of $\max\{ds/dt\}$. One can also see indication that the P_{99} of filtered accelerations can be scaled via power-law, to transform from one filter frequency to another. This is presumably useful for dealing with turbines having different control system response times. Although Nielsen *et al*. (2004) identified the need for a "3rd order filter to avoid cascading" whereby multiple jumps and accelerations (of decreasing scale) would inflate the count of events, they were concerned with wind speeds crossing above a given threshold (thus progressively zooming in to the threshold, at smaller and smaller scales more crossing-events can be found, unless one low-pass filters); here we are merely calculating the top 1% of accelerations per each period, and avoid such a constraint.

3.3.1. Towards a climatology of streamwise load-driving accelerations

The long-term probability density of 10-minute 99th-percentile accelerations is shown in Figure 3, for the two primary heights considered (100m and 160m above the sea), and for three different response times (inverse low-pass filter scales f_c^{-1} of 3, 10, and 30 seconds). This gives context for the earlier figure, showing that the right-hand plot of Figure 2 indeed corresponds to a period containing an extreme acceleration event, while the left-hand plot in Figure 2 corresponds to a period where the filtered acceleration falls in the peak (most common) of 10-minute $\dot{s}_{99}$; e.g. for a filter frequency of 0.1 Hz, the $\dot{s}_{99}$ at 160m are about 0.3 m/s^2 and 1 m/s^2, respectively.

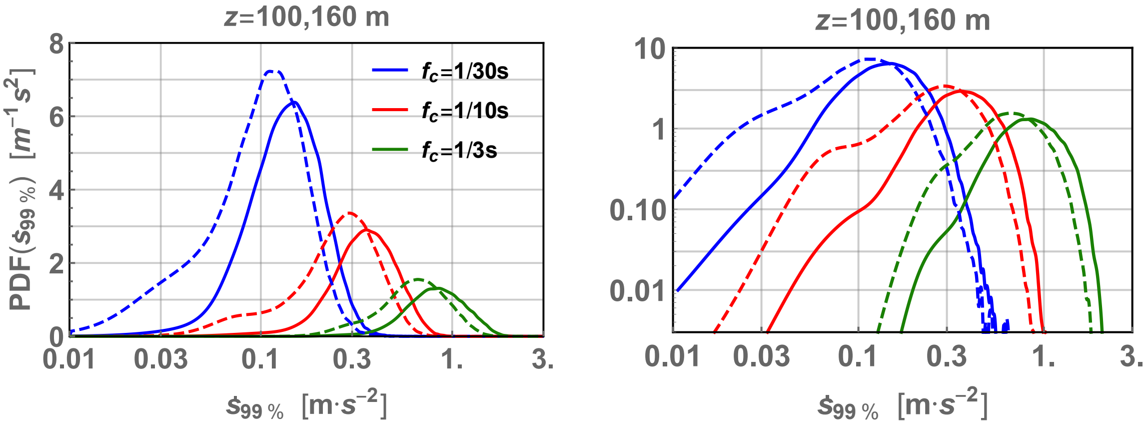

Figure 3. Long-term distribution of load-driving accelerations: PDF of 10-minute P_{99}'s of filtered ds/dt, for three different filter scales, from measurements at 100m (solid) and 160m height (dashed). Both semi-log (left) and log-log (right) shown for clarity.

Given that the range of wind speeds used occur 32.8% of the time in the range of wind speeds considered, if we assume that far offshore that the conditions in Figure 3 are representative for all directions, then the *number* of $\dot{s}_{99}$ values detected for a given 'bin' of acceleration will occur about 3.05 times more than detected; but we remind that the probability *density* $P(\dot{s}_{99})$ shown in the figure will not change. One can also see that higher $\dot{s}_{99}$ are seen at 100 m compared to 160 m, including the highest (extreme) accelerations. However, considering the works of e.g. Liu & Liang (2010) we note the possibility that due to the relative rareness of atmospheric boundary-layer [ABL] depths as shallow as 160 m (or 100 m), it is possible that for heights farther above from the water the accelerations could be larger—due to effects from the ABL-capping inversion (e.g. breaking gravity waves, turbulent entrainment).

The PDF of $\dot{s}_{99}$ follows a log-normal form quite well, particularly around the peak and on its right side, which we are more concerned with (our data selection has limited the left/small side of $P(\dot{s}_{99})$ already by choice). The PDF and log-normal fits are shown in Figure 4 below for low-pass frequency of 0.1Hz; here we obtained the log-normal parameters[4] $\{\mu_g, \sigma_g\} = \{-0.88, 0.36\}$ for 100 m and $\{-1.1, 0.38\}$ for 160 m height for this f_c.

---

[4] Recall that for log-normal distributions, the parameters $\{\mu_g, \sigma_g\}$ denote the geometric (multiplicative) mean and geometric standard deviation.

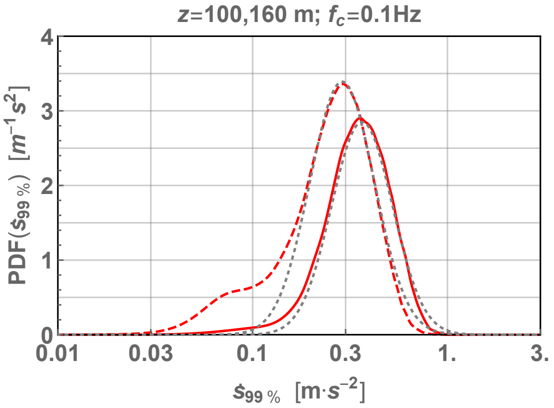

Figure 4. Left: PDF of $\dot{s}_{99}$ for z=100m (solid red) and z=160m (dashed red); log-normal fits are dotted gray.

We note however, that the 20-30 most extreme $\dot{s}_{99}$ recorded at both heights deviate markedly from the fitted log-normal form, and the figure also shows that the log-normal distribution fit around the peaks gives rise to overprediction of the extremes (tails "too fat"). But adjusting $\{\mu_g, \sigma_g\}$ to $\{-0.75, 0.22\}$ and $\{-1.0, 0.26\}$ for 100 m and 160 m heights, respectively for $f_c = 0.1$ Hz, we can see that the extremes are better fit. This is shown by plotting the survival function (1–CDF) in log-log coordinates, as depicted in Figure 5.

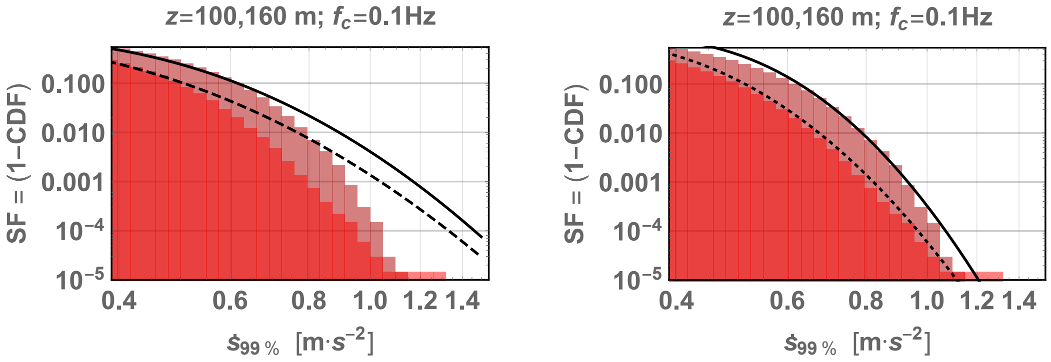

Figure 5. Survival function (SF=1–CDF) of $\dot{s}_{99}$ from observations at 100 m (dark red) and 160 m (red), for f_c=0.1Hz; lines show the fitted log-normal SF for 100 m (solid) and 160 m (dashed). Left: SF for center-based fits from Fig.4. Right: fits updated to capture observed extreme values.

From the fitted distributions one can estimate return-rates, and also the expected 50-year value of 10-minute $\dot{s}_{99}$, by inverting the log-normal distribution function and scaling for the number of observations (years) that we have taken to get the distribution (including an omnidirectional assumption). Doing so gives us 50-year estimates of $\dot{s}_{99}$ equal to approximately 1.3 m/s for 100 m, and 1.2 m/s for 160 m height, for the case of a 10 s characteristic response time (low-pass filter scale $f_c = 0.1$ Hz).

For shorter characteristic turbine response times (higher filter frequencies), the extreme accelerations are larger, and for lower f_c the opposite happens. Figure 6 shows the survival function (1–CDF) of the largest $\dot{s}_{99}$ for all three filter scales (response times) considered, i.e., $f_c = \left\{\frac{1}{30}, \frac{1}{10}, \frac{1}{3}\right\}$ Hz.

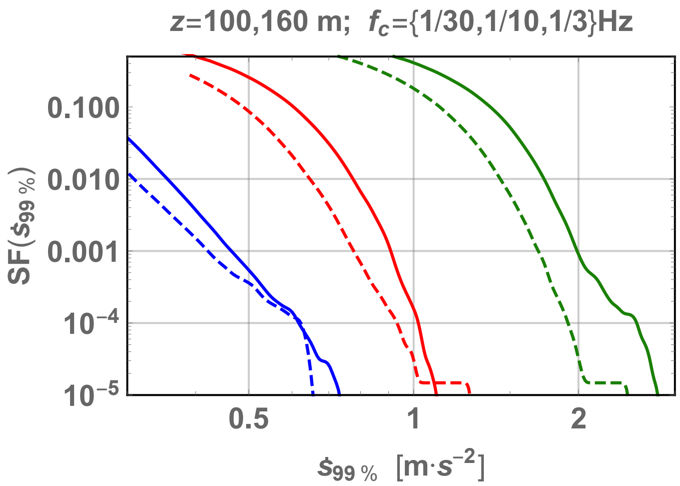

Figure 6. Observed SF (i.e., 1–CDF) in the extreme range for different low-pass filter scales, $f_c = \{1/30, 0.1, 1/3\}$ *Hz.*

Just as we obtained $\{\mu_g, \sigma_g\}$ at 100 m and 160 m heights with $f_c = 0.1$ Hz, we also obtain corresponding values for the other low-pass filter scales considered, i.e. for $f_c = 1/30$ Hz and 1/3 Hz; these are shown in Table 1 below.

Table 1. Fitted log-normal distribution parameters for extrapolation of extreme accelerations.

	$f_c = (1/30)$ Hz	$f_c = 0.1$ Hz	$f_c = (1/3)$ Hz
$\{\mu_g, \sigma_g\}$ at 100 m height:	$\{-1.9, 0.38\}$	$\{-0.75, 0.22\}$	$\{-0.08, 0.26\}$
$\{\mu_g, \sigma_g\}$ at 100 m height:	$\{-2.1, 0.41\}$	$\{-1.0, 0.26\}$	$\{-0.24, 0.24\}$

From log-normal distributions with the parameters shown in Table 1, one may construct plots of expected 10-minute $\dot{s}_{99}$ per return period. These are shown in Figure 7. Expected maximum 10-minute $\dot{s}_{99}$ for a given return period, for different timeseries low-pass filter frequencies (inverse characteristic response times), at 100 m and 160 m height; based on log-normal fits to tails of PDFs of $\dot{s}_{99}$..

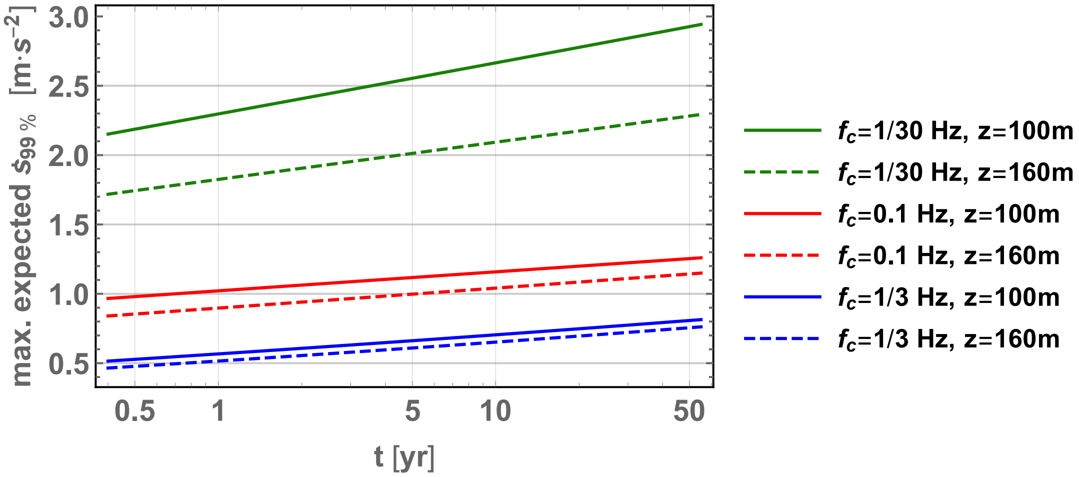

Figure 7. Expected maximum 10-minute $\dot{s}_{99}$ *for a given return period, for different timeseries low-pass filter frequencies (inverse characteristic response times), at 100 m and 160 m height; based on log-normal fits to tails of PDFs of* $\dot{s}_{99}$*.*

We note these values correspond only to the range of wind speeds considered, between 8–17 m/s. A logical follow-up would be to find extreme $\dot{s}_{99}$ conditioned on wind speed: i.e., fits like the above, but for individual wind speed bins. However, as will be seen in a later section, no dependence of the extreme accelerations on wind speed is observed; further, there smaller number of data points per wind speed bin cause more difficulty and larger uncertainty in fitting such conditional distributions.

3.3.1.1. 10-minute statistics and relatability to load-driving accelerations

As mentioned earlier in the background section, load-driving acceleration events themselves cannot be detected directly from 10-minute statistics, such as the standard deviations of wind speed (σ_s) or streamwise velocity (σ_u). However, one expects some relation between σ_s and the $\dot{s}_{99}$ (or alternately σ_u and $\dot{u}_{99}$); larger accelerations which are significantly long should cause higher standard deviations of wind speed. Figure 8 shows the joint PDF of 10-minute $\dot{s}_{99}$ and σ_s at both 100 m and 160 m heights.

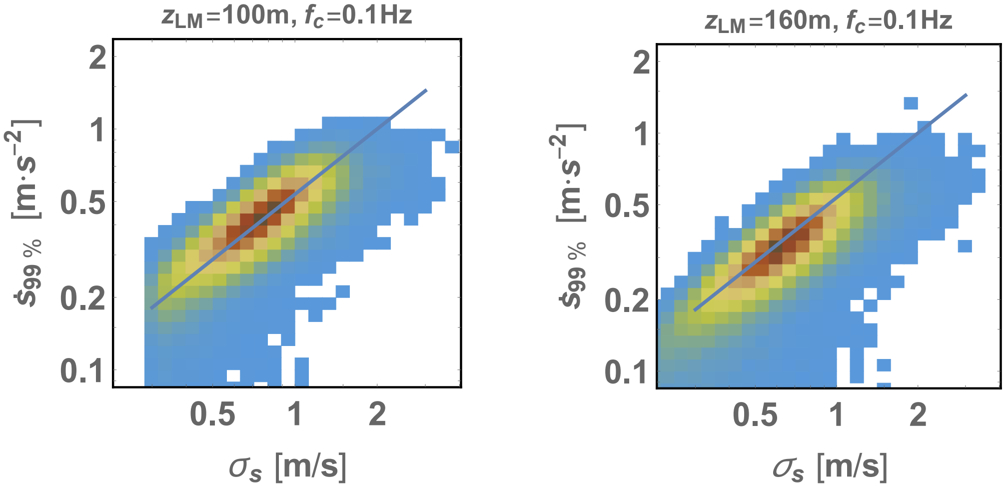

Figure 8. Joint PDF of all 10-minute top (99th percentile) low-pass filtered accelerations (f_c=0.1 Hz) and standard deviation of wind speed, for both 100 m and 160 m heights. Straight lines: linear fits based on mode of $\dot{s}_{99}$.

From the figure one can quickly confirm two things. First, one sees that the extreme streamwise accelerations do not correlate with σ_s for $\sigma_s \gtrsim 1$ m/s (flat upper edge of colored area). Secondly, the most common 10-minute top 1% accelerations conditioned on σ_s (e.g. the mode of $\dot{s}_{99}$ given by the solid line) shows a linear relationship with σ_s, in the range of common σ_s (i.e. for σ_s below 1.5 m/s). In other words, the most common 10-minute maximum accelerations are proportional to the 10-minute standard deviation of wind speed. This sane result gives fundamental support to the use of σ_s for fatigue loads by the IEC 61400-1 standard: it is essentially taking σ_s to be a proxy for the accelerations dominating each 10-minute period.

Further, we note that the results are qualitatively the same as in Figure 8, if one filters with larger and smaller filter frequencies, i.e. for faster or slower turbine characteristic-response times. This is demonstrated by Figure 9 below.

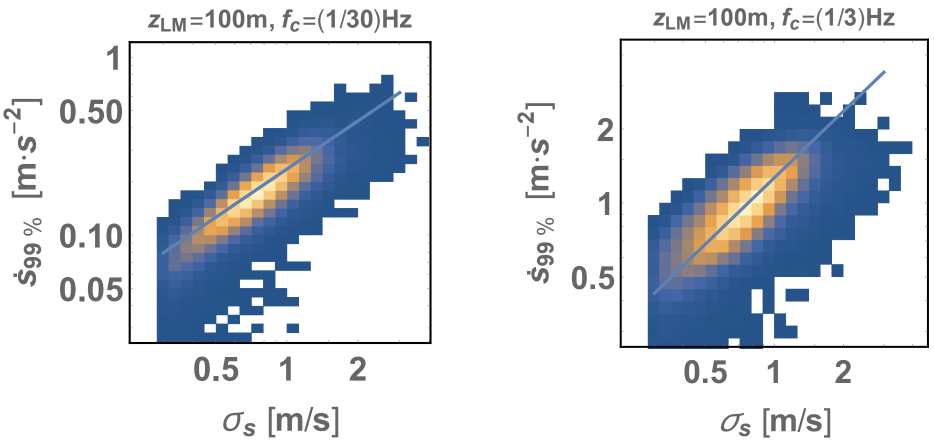

Figure 9. Joint PDF of all 10-minute top (99th percentile) low-pass filtered accelerations and standard deviation of wind speed, for both 100 m heights. Left: filter scale f_c=1/30 Hz; right: filter scale f_c=1/3 Hz. Straight lines: linear fits from mode$\{\dot{s}_{99}|\sigma_s\}$.

In Figure 9 one sees again a linear fit of the most common 10-minute low-pass filtered $\dot{s}_{99}$ versus σ_s (via the mode of $\dot{s}_{99}$), for low-pass filter frequencies of $\frac{1}{30}$ Hz and $\frac{1}{3}$ Hz. As for the case shown in Figure 8 having f_c =0.1 Hz, this line and these accelerations basically correspond to fatigue loads. Additionally, we find that

$$\text{mode}\{\dot{s}_{99}|\sigma_s\} \simeq (c\sigma_s)^{0.9}, \quad \text{where} \quad c = \left(\frac{0.044\ \text{Hz}}{f_c}\right)^{0.8}. \tag{1}$$

In contrast, for the extremes, which occur for $\sigma_s \gtrsim 1$ m/s, there does not appear to a clear relationship between max$\{\dot{s}_{99}|\sigma_s\}$ and the standard deviation of wind speed σ_s; Figs. 8 and 9 both show flattening of the $\{\dot{s}_{99}, \sigma_s\}$ envelope for the largest $\dot{s}_{99}$. However, it is possible that this is a sampling issue, whereby a larger data set (longer measurement period) could show an extension of the jPDF shapes further towards the upper right (higher $\{\dot{s}_{99}, \sigma_s\}$) in the above two figures.

A number of previous works (e.g. Moriarty *et al.*, 2004; Nielsen *et al.* 2004) have also stated or presumed that load-driving events tend to be associated with non-Gaussian turbulence. Thus in Figure 10 below, we display the joint distributions of both skewness and kurtosis with $\dot{s}_{99}$.

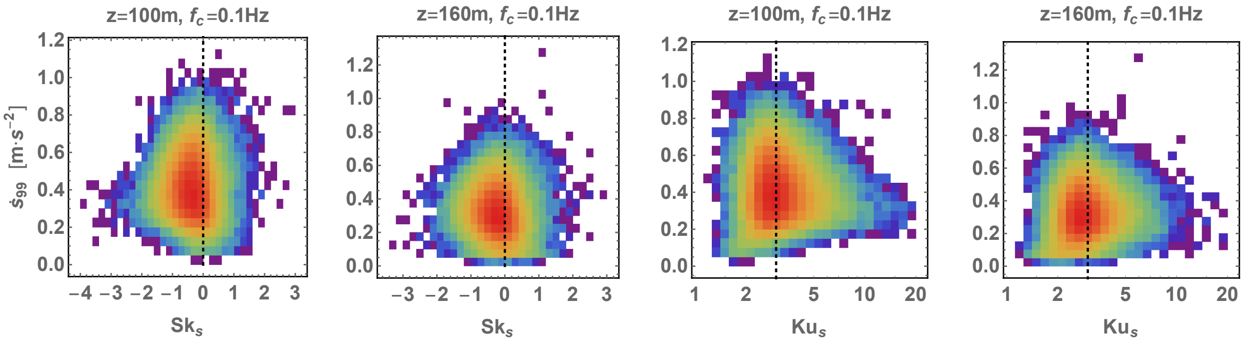

Figure 10. Joint PDF of filtered max-like accelerations $\dot{s}_{99}$, with either Skewness or Kurtosis of wind speed; results shown for both 100 m and 160 m heights. Logarithmic scale used for jPDF colors. Dotted lines denote Gaussian values, Sk$_s$=0 *and* Ku$_s$=3*, respectively.*

Figure 10 shows that the dominant accelerations $\dot{s}_{99}$ exhibit no apparent association with 10-minute skewness or kurtosis. One can see that the most common events are nearly Gaussian, with a kurtosis of 3, however with a slightly negative skewness. The stronger events also appear to be essentially centered around Gaussian values for skewness and kurtosis (dotted lines in the plots), but with a larger fraction of stronger events appearing as non-Gaussian outliers.

In addition to the climatological (long-term) bulk relationship between the most common (fatigue) load-driving accelerations $\dot{s}_{99}$ and σ_s depending on filter scale according to equation 1 above, we also note that within a given 10-minute period the skewness and kurtosis can have more complicated dependences upon the low-pass filter scale; this is shown in Figure 11 below. However, we also remind that the *dimensionless* sensitivity of the amplitude of most common filtered accelerations to σ_s does not depend on filter scale, since (1) also gives $d\ln(\text{mode}\{\dot{s}_{99}\})\,/d\ln\sigma_s = 0.9$.

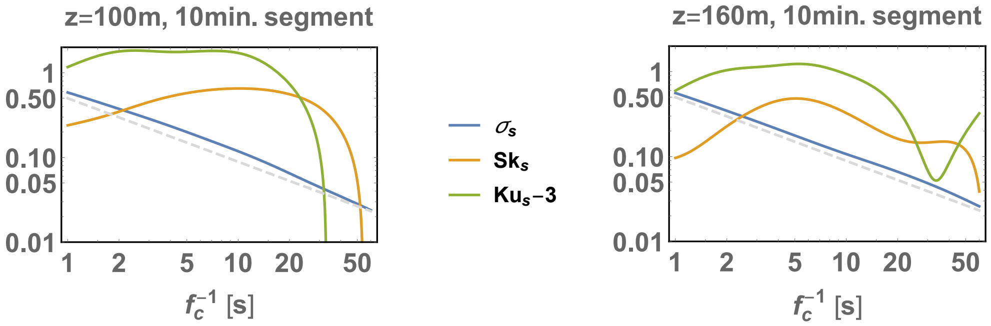

Figure 11. Sample 10-minute period showing dependence of standard deviation, skewness, and kurtosis of wind speed on low-pass filter scale (f_c).

One last demonstration of the statistical (long-term) effect of filter scale on the load-driving accelerations can be seen by comparing P_{99} of the accelerations calculated for every 10-minute period but filtered with different low-pass frequency; Figure 12 shows this.

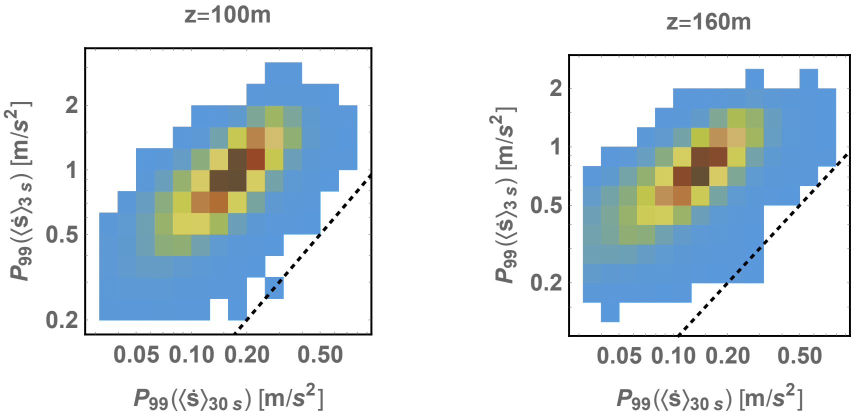

Figure 12. Joint PDF of all 10-minute 99th percentiles of low-pass filtered accelerations, using filter scales fc=1/(3s) and 1/(30s), respectively. Left: result at 100 m height; right: result for 160 m height. Dotted line indicates 1:1 relationship.

The figure displays the load-driving accelerations filtered with a timescale of 3s versus those filtered with a timescale of 30s calculated as the 99th percentile for each 10-minute period, in terms of their jPDF. It essentially shows that different filter scales lead to different apparent accelerations—and events, and a simple linear relationship does not arise; however, longer response times (lower filter frequencies) do lead to smaller $\dot{s}_{99}$, as shown by the dotted (1:1) line in the figure.

3.3.1.2. Spatially differential acceleration: difference from hub to tip

In addition to accelerations at 100 m and 160 m, respectively, we also consider shear-like situations which are due to a large difference in acceleration over a vertical (60 m) span. Figure 13 shows the joint distribution of 99th percentile of vertical acceleration gradient with a number of other relevant quantities: $\dot{s}_{99}$, σ_s, and sub-mesoscale σ_s. Following Hannesdóttir & Kelly (2019), a 2nd-order *spatial high-pass* Butterworth filter was also applied (via Taylor's hypothesis with a spatial filter scale of 2 km), to separate mesoscale and sub-mesoscale motions; for some quantities, as will be seen in later sections, these spatially different components correlate differently with load-driving accelerations.

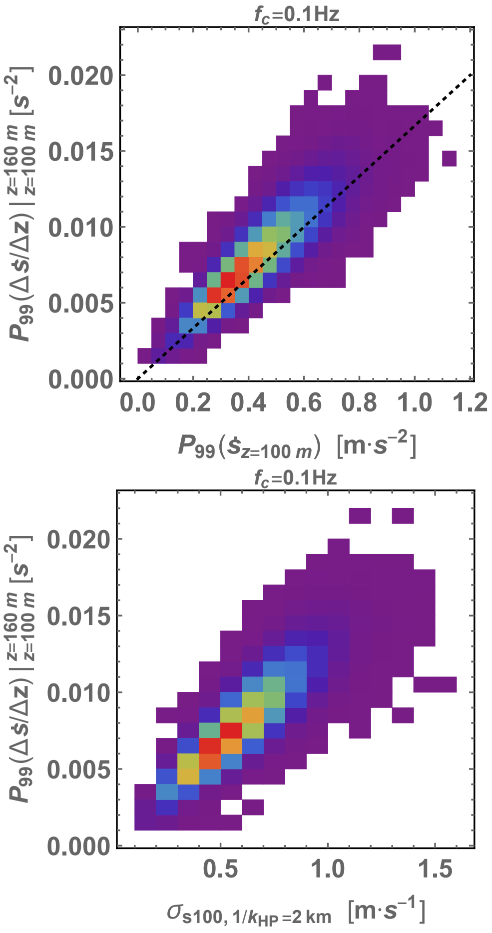

Figure 13. Joint PDF of P_{99} of vertical gradient of accelerations: joint with $\dot{s}_{99}$ at 100 m height (upper-left), 10-minute σ_s at 100 m height (upper-right), and sub-mesoscale 10-minute σ_s at 100 m (bottom). Dotted line in upper-left plot is 60:1, corresponding to acceleration difference equal to acceleration at 100 m..

From the upper-left plot of the figure above one can see that the 99th-percentile filtered accelerations ($\dot{s}_{99}$) at 100 m tend to coincide with 99th-percentile of differences in $\dot{s}$ between 100 and 160 meters;

multiplying its vertical axis by 60 (or looking at the dotted line), one can see that most commonly the acceleration difference is greater than 0, more so for larger accelerations. Extreme differences in acceleration are approximately twice as large as the corresponding accelerations at 100 m; flap-wise root bending moments can be significantly impacted by this. Figure 13 also shows that σ_s at 100 m (i.e. at common hub heights) does not correlate that well with the load-driving P99 of filtered acceleration gradients, while the sub-mesoscale part of σ_s, i.e. spatially high-pass filtered (while also being temporally low-pass filtered), can serve as a better proxy for the most common (fatigue-driving) acceleration differences.

We also note that this analysis has not tried to address the effect of coherent structures tilted from the vertical (e.g. ramp-like events detected by Hannesdóttir *et al*. (2017), which would involve a time-lag between large accelerations occurring at two heights. Aside from very small lags considering typical blade deflections, this is assumed to be insignificant (though could be studied in the future).

3.3.2. Directional / cross-wind accelerations and climatology

Following the streamwise (out-of-plane) load-inducing accelerations considered in the previous sections, here we consider lateral (cross-wind) accelerations, expressible as the time rate of change of direction $\dot{\varphi} = d\varphi/dt$. Again the derivatives calculated in the Fourier domain, as with the wind speeds analyzed above.

Given the longer timescales that tend to be involved in directional changes compared to speed changes, we apply a *spatial* filter to decompose our timeseries into mesoscale and sub-meso components, as in Hannesdóttir & Kelly (2019); this is also done using a 2$^{\text{nd}}$-order Butterworth filter, but instead of having a constant filter frequency, $f_c = S/(2\text{km})$ is used, where S is the mean wind speed. Thus both a long- and short-scale spatial filter (i.e. low- and high-pass in wavenumber space) is applied to timeseries, allowing us to examine the behavior of directional accelerations with regard to spatial scale, as illustrated in Figure 14.

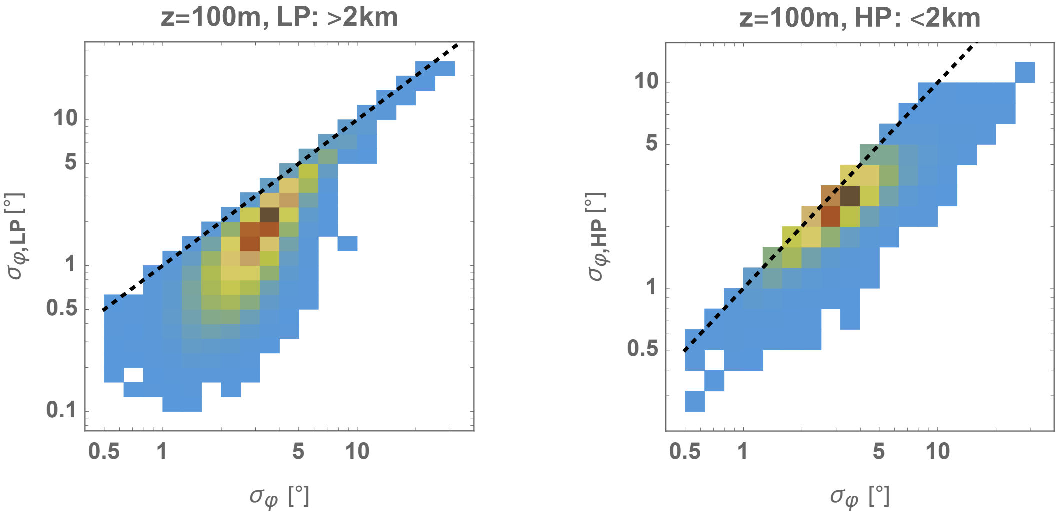

Figure 14. Standard deviations of spatially low-pass (left) and high-pass filtered (right) wind direction, versus full standard deviation; filter scale is 2km, Yamartino method used to calculate all standard deviations. Dotted lines show 1:1 relation.

The figure above shows the standard deviation of 'mesoscale' direction (spatially low-pass filtered, fluctuations at scales mostly greater than ~2km) and 'sub-meso' direction (fluctuations at scales smaller than ~2km) timeseries. The Yamartino (1984) method is used to calculate all standard deviations of wind direction herein. From the figure one can see that the largest standard deviations are mostly caused by fluctuations and structures having scales larger than ~2km, particularly for $\sigma_\varphi \gtrsim 10°$.

Unlike the wind speed, large changes in direction at current rotor heights appear to be more associated with mesoscale structures—and not turbulence. However, this may not be the case for directional (lateral) accelerations; this is borne out when considering the statistics of 10-minute P_{99} of temporally low-pass filtered directional acceleration $\dot{\varphi}$, as shown in Figure 15 below.

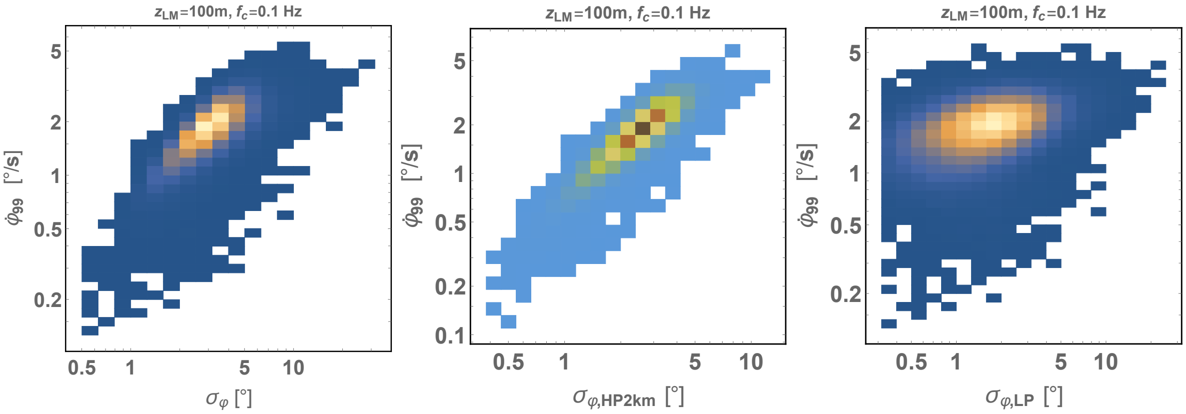

Figure 15. Joint PDF of 99th percentile of temporally low-pass filtered directional acceleration $\dot{\varphi}$ with standard deviation of direction (left), sub-mesoscale φ (center), and mesoscale φ (right). All are taken from data at a height of 100 m.

As shown above in Figure 15, the largest lateral accelerations tend to be more correlated with sub-mesoscale fluctuations; the standard deviations of high-pass spatially filtered directional timeseries are more correlated to $\dot{\varphi}_{99}$ than the mesoscale (spatial low-pass) or full standard deviation. Moreover, the mode of $\dot{\varphi}_{99}$ conditioned on $\sigma_{\varphi(k>2\pi/2\mathrm{km})}$ is linear in the latter, as seen in the center plot; this is analogous to the behavior of the most common maximum streamwise accelerations $\dot{s}_{99}$ being proportional to σ_s as shown in Figure 8. While Figure 15 shows results from observations at 100 m, the same is also found for data recorded at 160 m (not shown); further, similar behavior is seen using filter frequencies of 1/(30s) or 1/(3s), just as was the case for streamwise accelerations.

3.3.3. Ultimate and fatigue-causing acceleration events

For practical use and possible comparison to (or adoption by) wind turbine standards, it is relevant to examine the behavior of load-causing events conditional on the mean wind speeds at which they occur; in particular, events near or crossing rated speed tend to induce greater loads during normal operation (e.g., Kelly *et al.*, 2021). Towards this end, to investigate the nature of events (potentially) driving both/either fatigue-inducing and ultimate loads, below we consider the joint probability of 10-minute 99th percentiles of low-pass filtered acceleration $\dot{s}$ and wind speed; this is displayed in Figure 16.

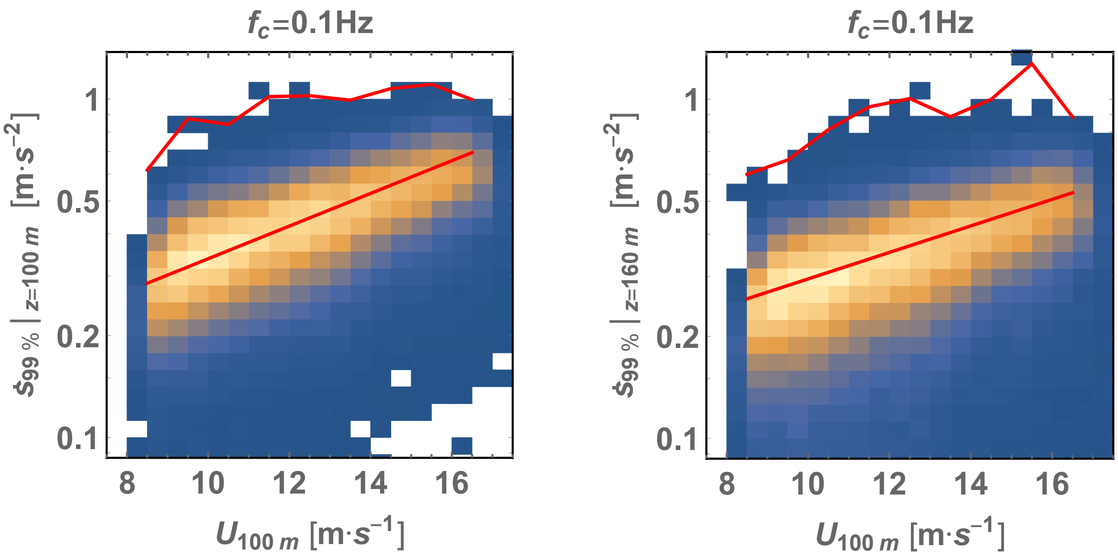

Figure 16. Joint PDF of top-1% temporally low-pass filtered accelerations (with f_c=0.1 Hz), and 10-minute mean wind speed at 100 m. Left: events and accelerations from 100 m height; right: from 160 m height. Straight red lines indicate mode of $\dot{s}_{99}$ conditioned on speed; jagged red line at top shows maximum (extreme) filtered accelerations.

Analogous to the behavior of $\dot{s}_{99}$ conditioned on σ_s (as in Figure 8), the mode of $\dot{s}_{99}|S$ is monotonic in S. This is shown in the figure above, where for practicality we show both the 100 m and 160 m accelerations conditioned on/joint with the speed at 100 m (a common choice for hub height). Based on the 100 m wind speed, the mode of $\dot{s}_{99}|S$ at 100 m (red line in left-hand plot above) is $(0.11\mathrm{ms}^{-2})e^{S_{100}/(9\ \mathrm{m/s})}$, while at 160 m $\mathrm{mode}\{\dot{s}_{99}|S\} \simeq (0.12\mathrm{m/s}^2)e^{S_{100}/(11\ \mathrm{m/s})}$. In terms of the speed at 160 m, the latter is nearly the same: a coefficient of $0.11\mathrm{m/s}^2$ is found, instead of 0.12; the log-slope is still dictated by a velocity scale of 11m/s. The velocity scales (9 or 11 m/s) are likely related to the long-term mean speed at each height, though this is a topic of future study.

One could argue that in a limited range around or below rated speed, the climatologically most common values of 10-minute 99th-percentile filtered accelerations, at *both* heights, are proportional to wind speed at 100 m. I.e., for $S < V_{\mathrm{rated}}$ the exponential can be approximated by a linear function in S; this would be consistent with (and partly explain) fatigue loads being proportional to mean wind speed at hub-height.

On the other hand, the *extreme* accelerations have not shown a clear trend with mean wind speed, though it is possible that with more data one might see the most extreme $\dot{s}_{99}$ showing some increase with S.

Comparing to the accelerations $\dot{s}_{99}$ calculated at 100 m with f_c=0.1 Hz shown in the left-hand plot of Figure 16 above, we can see analogous results occurring for lower and higher filter frequencies, i.e., for f_c=1/30 Hz and 1/3 Hz, respectively; this is shown in Figure 17 below. As expected, both the most common and extreme 10-minute max accelerations $\dot{s}_{99}$ are larger for higher low-pass filter frequencies (shorter averaging times) and smaller for lower f_c. Just as with equation (1) for the mode conditioned on 10-minute σ_s, the dependence of $\partial(\mathrm{mode}\{\dot{s}_{99}|S\})/\partial S$ on f_c can be expressed with a simple power-law dependence.

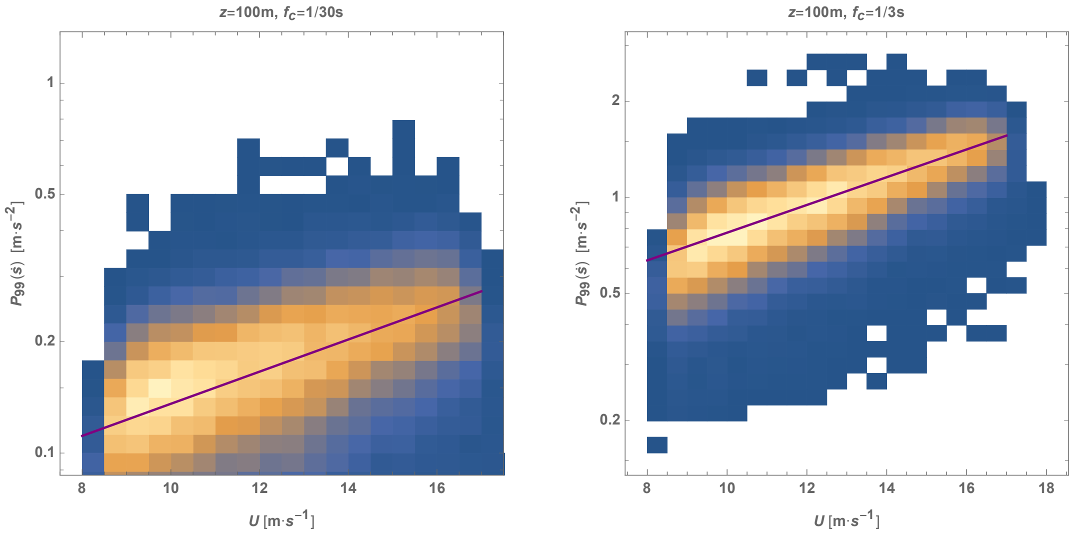

Figure 17. Joint PDF of top-1% temporally low-pass filtered accelerations and 10-minute mean wind speed at 100 m height. Left: filtering with f_c=1/30 Hz; right: filtering with f_c=1/3 Hz. Straight red lines indicate mode of $\dot{s}_{99}$ conditioned on speed.

3.3.3.1. Timeseries of streamwise-acceleration events

The ten most extreme streamwise acceleration events were detected per wind speed bins of 1 m/s width, ranging from 8–17 m/s, at both 100 m and 160 m heights. I.e., 180 (10*9*2) streamwise acceleration events were detected, with the corresponding timeseries of streamwise and lateral velocity (and speed and direction) saved for later use in constrained turbulence simulations to drive aeroelastic loads in WP3-4. The most extreme in each wind speed bin is shown in Figure 18 below. For brevity and compactness, each plot in the figure shows two events per wind speed bin: the most extreme event detected at 100 m, and the one detected at 160 m; further, each plot shows the speed at both heights for each event, resulting in 4 lines. The events/plots shown are for a low-pass filter frequency of 0.1 Hz, as with the main figures presented earlier.

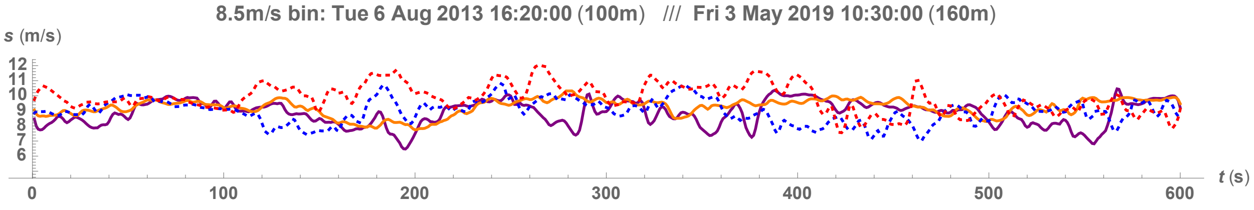

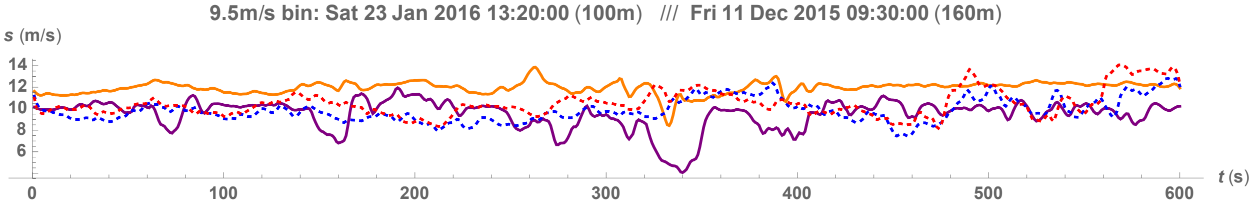

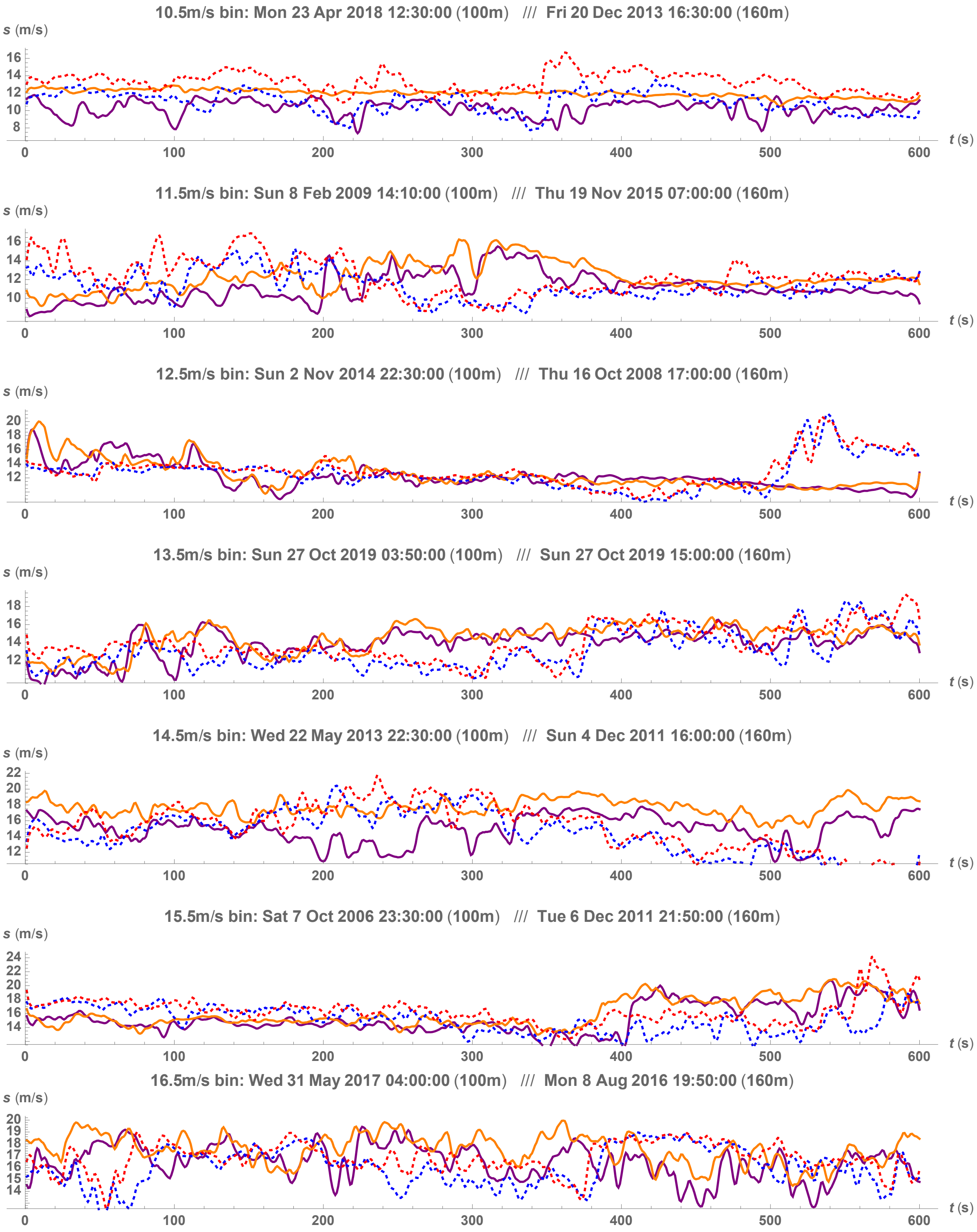

Figure 18. Timeseries of wind speed for largest wind acceleration event detected in each wind mean speed bin, where speed bins are 1 m/s wide with centers ranging from 8.5 to 16.5 m/s. Solid lines are each extreme event detected at 100 m, with $S_{100\,m}$ in purple and $S_{160\,m}$ in orange; dotted lines are for each extreme event found at 160 m, with $S_{100\,m}$ in blue and $S_{160\,m}$ in red.

The most extreme events per mean wind speed bin (1 m/s width from 8–17 m/s) detected at 100 m were different than those at 160 m, as seen in Figure 18 above. As can be inferred from the timeseries shown, a number of different qualitative properties and corresponding meteorological phenomena are associated with these extreme events. First, for some of the 100 m events (solid lines in Figure 18) one can see that the corresponding 160 m speeds are either constant or look like a smoother version of the 100 m speed, particularly for smaller mean speed bins (below rated). These correspond to shallow ABL depths (which typically occur during winter or nighttime) where the anemometer at 160 m height is near or within the stable inversion where turbulence is suppressed; the cases with $S_{160\text{ m}}$ following $S_{100\text{ m}}$ tend to correspond to being just below the inversion, with either breaking gravity waves or entrainment-zone turbulence (offshore convective cells could give a similar signature but were ruled out by checking the corresponding vertical velocity timeseries). The cases with 'flat' $S_{160\text{ m}}$ correspond to shallow ABL depths below 160 m. At higher speeds (above ~11m/s) the extreme acceleration events at 100 m also tended to be accompanied by significant accelerations at 160 m, which is consistent with the irregular spatial structure of the ABL-capping inversion (e.g. Wyngaard, 2010). Unfortunately, consistent ceilometer data from Høvsøre were not available for these events to quantify the ABL depths.

For the top extreme events detected at 160 m (dotted lines in Figure 18), the acceleration-associated jumps in wind speed were accompanied by similar fluctuations at 100 m, consistent with ABL depths near or just above 160 m. Further, for some of these events one can also see steady winds before or after the jumps, commensurate with inversion depths fluctuating around this height. For several bins there was also nonstationarity at both heights, occurring during daytime hours, consistent with frontal passage; this included two wind speed ramp events.

Further identification of these events may be accomplished through mesoscale simulations and analysis carried out by UiB during the course of WP2-3. Timeseries of these events—additionally the top 10 events in each mean-speed bin—have been provided for aeroelastic simulations in WP3–4, along with the corresponding Mann-model parameters (see later sections); the timeseries are provided as downsampled (1 Hz) records of speed, direction, streamwise velocity component, and lateral velocity component, at both 100 m and 160 m heights.

3.3.3.2. Directional (crosswind) acceleration events

In addition to the wind-speed (streamwise) extreme acceleration events shown above, here we present the analogous directional acceleration events. While analyzed both in terms of streamwise/lateral velocity components and windspeed/direction, in Figure 19 below we show the timeseries of wind direction for the most extreme $d\varphi/dt$ in each mean wind speed bin, with the 100 m and 160 m events shown together in each plot. Thus each plot contains two pairs of lines, with each pair (solid or dotted) corresponding to an event at either 100 m or 160 m.

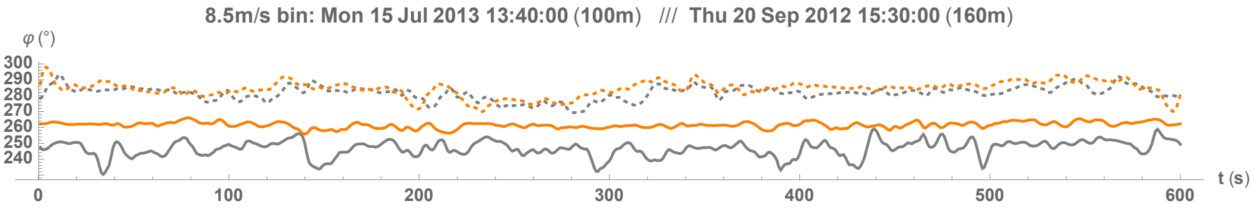
8.5m/s bin: Mon 15 Jul 2013 13:40:00 (100m) /// Thu 20 Sep 2012 15:30:00 (160m)

9.5m/s bin: Sat 23 Jan 2016 13:20:00 (100m) /// Wed 22 Mar 2006 21:00:00 (160m)

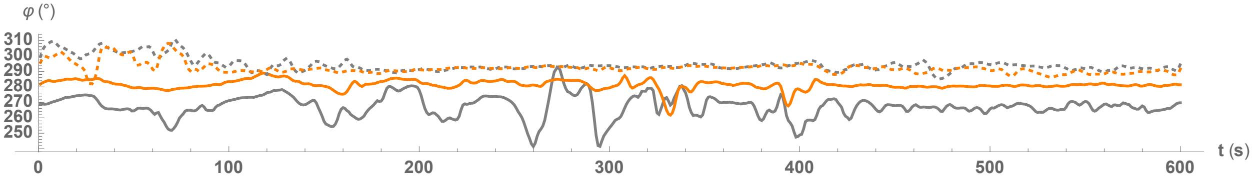

10.5m/s bin: Sat 17 Sep 2005 22:10:00 (100m) /// Sat 12 Jun 2010 01:30:00 (160m)

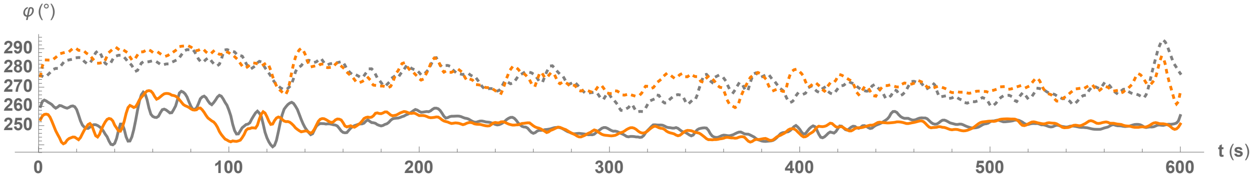

11.5m/s bin: Thu 19 Nov 2015 07:00:00 (100m) /// Thu 19 Nov 2015 07:00:00 (160m)

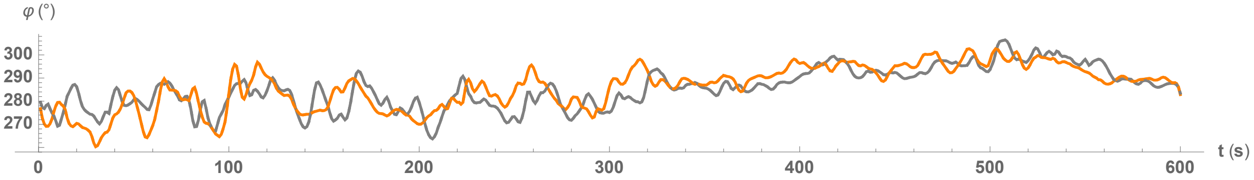

12.5m/s bin: Sun 30 Aug 2009 09:30:00 (100m) /// Fri 21 Jan 2005 18:30:00 (160m)

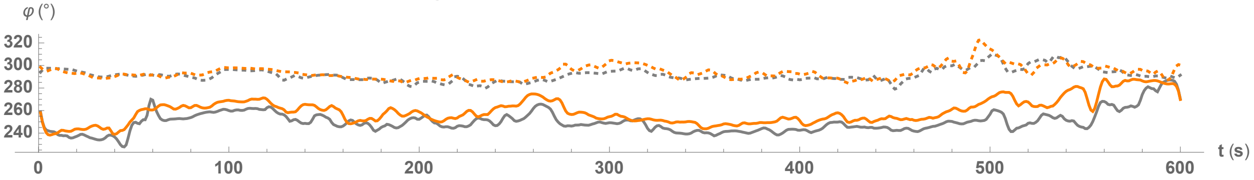

13.5m/s bin: Tue 11 Feb 2020 22:10:00 (100m) /// Sun 1 Sep 2013 16:40:00 (160m)

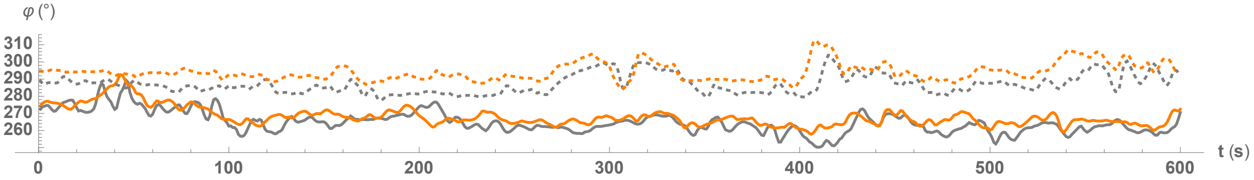

14.5m/s bin: Sat 9 Mar 2019 06:30:00 (100m) /// Sat 18 Nov 2017 03:10:00 (160m)

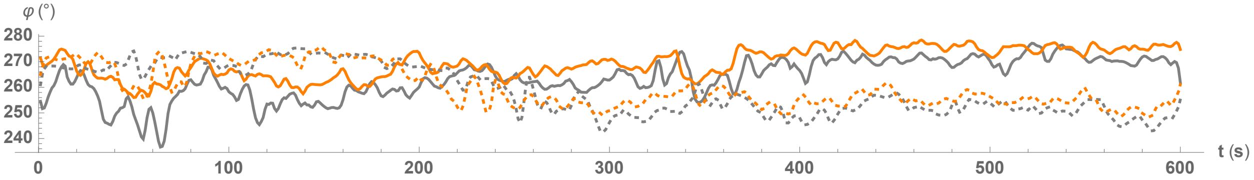

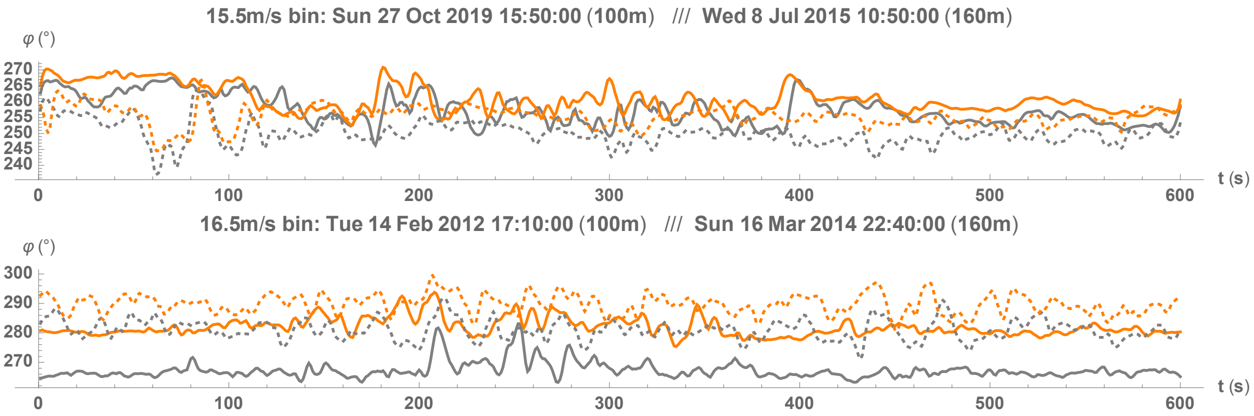

Figure 19. Timeseries of wind direction for largest directional (lateral) acceleration event detected in each wind mean speed bin, where speed bins are 1 m/s wide with centers ranging from 8.5 to 16.5 m/s. Solid lines are each extreme event detected at 100 m; dotted lines are for each extreme event found at 160 m. Gray is $\varphi_{100\text{ m}}$ *and orange is* $\varphi_{160\text{ m}}$*; thus solid gray and dotted orange, respectively, are the basis for the two events shown in each plot.*

From the direction timeseries for the bin-wise extreme lateral accelerations shown in Figure 19, several things stand out. First, many of the extreme lateral accelerations bear some qualitative resemblance to their streamwise counterparts: many events detected at 100 m are accompanied by direction timeseries at 160 m which are either steady or look like a smoothed version of the 100 m direction; for these we postulate the same meteorological mechanisms as attributed and described in the previous section for streamwise acceleration events. The lack of veer for some of these events also supports the inversion depth being near but above 160 m, such that entrainment-induced turbulence is mixing away any difference in flow direction. The 100 m events where the 160 m direction is steady also exhibit a noticeable veer, consistent with the inversion height being between 100 and 160 m. A few events at either 100 m or 160 m also appear to be associated with frontal passage, where the direction gradually changes over the 10-minute period. Finally, one of the bin-wise extreme directional acceleration events happens at both 100 m and 160 m heights during the same time period (the 11–12 m/s bin, on Nov. 15, 2015); this same event is also the extreme for 160 m streamwise acceleration, as can be seen in Figure 18.

Yet more relevant for the lateral acceleration events is one fundamental difference they appear to have, compared to streamwise accelerations: their independence of wind speed. This is shown in Figure 20 below. From the figure one can see that the lateral acceleration is constant across mean speeds, with a value of 2°/s at 100 m height and 1.6°/s at 160 m.

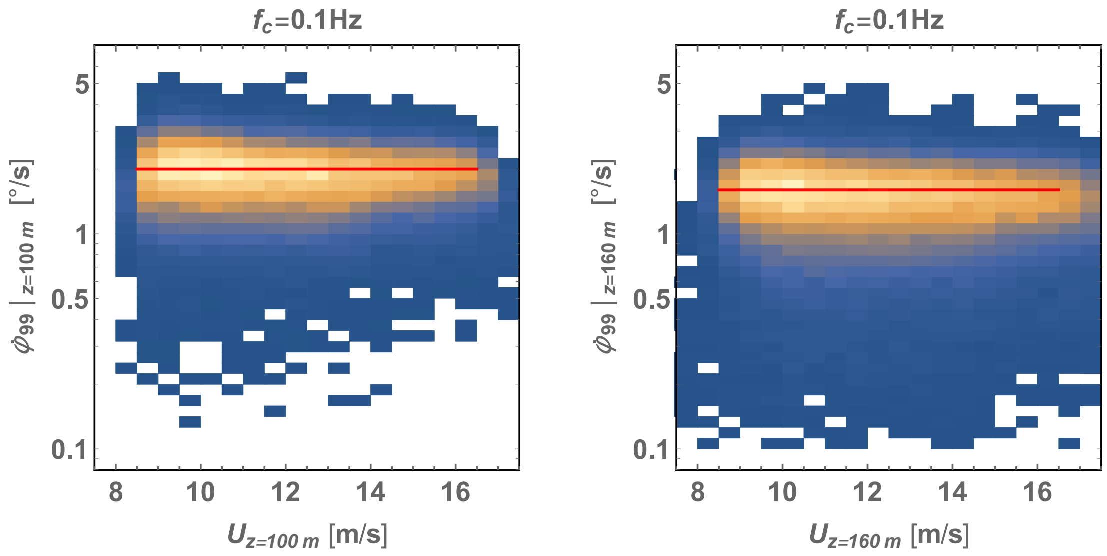

Figure 20. Joint histogram of filtered lateral accelerations (plotted as $\dot{\varphi}$*) and mean wind speed, for low-pass filter scale* f_c*=0.1Hz. Left: 100 m height; right: 160 m height.*

3.3.4. ‘Anatomy’ of a load-inducing acceleration event

One potentially useful way of visualizing the extreme events is to consider the streamwise and lateral accelerations together, over a 10-minute period. Figure 21 shows the lateral versus streamwise acceleration for the extreme event which for speeds between 11–12 m/s gave the maximum filtered $d\varphi/dt$ (and dv/dt) at both 100 m and 160 m height, as well as the maximum ds/dt (and du/dt) at 160 m.

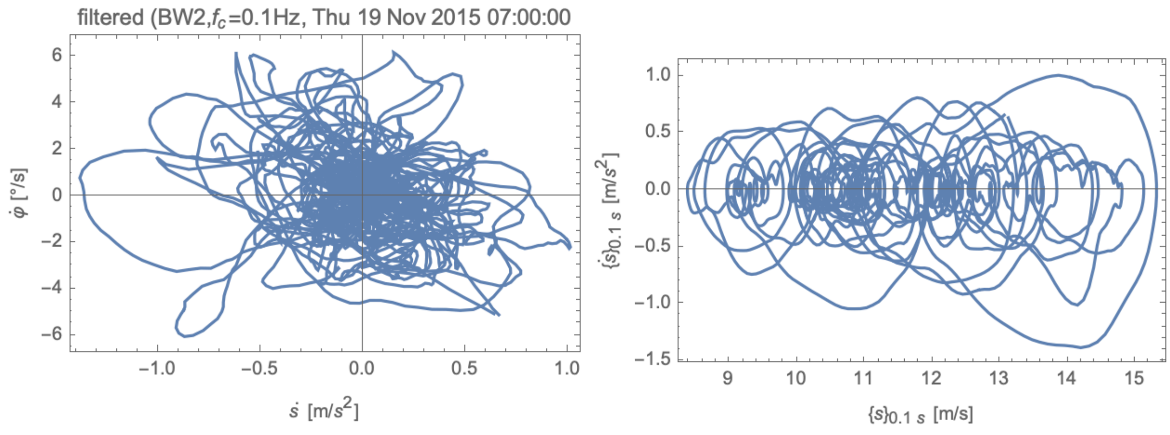

Figure 21. Acceleration space for an extreme event at 100 m height. Left: accelerations in terms of speed and direction; right: filtered streamwise accelerations and speed. Each plot is 10 minutes of filtered data, with each dot corresponding to 0.1 s; here a low-pass filter frequency of 0.1 Hz was used.

The figure displays how the vector acceleration evolved for the most extreme event at 100 m height in the 11–12 m/s bin; a number of large accelerations occur, ranging from lateral to streamwise directions. The streamwise component of acceleration was larger than the lateral component for most of the large accelerations (i.e. plotting $\dot{v}$ versus $\dot{u}$, not shown). We remind that the largest excursions only indirectly affect the 99th percentile value of $\dot{s}$ and $\dot{\varphi}$; e.g. $\dot{s}_{99} < 1$ m/s^2 here. However, we also note from the right-hand plot that such an ‘event’ will involve speeds crossing above and below rated speed multiple times (for current multi-megawatt turbines).

A more typical 10-minute period is shown below in Figure 22, from 160 m height when the mean wind speed was about 14 m/s. As with the extreme event from the previous figure, one can again see the observed filtered acceleration meandering from streamwise to lateral and between.

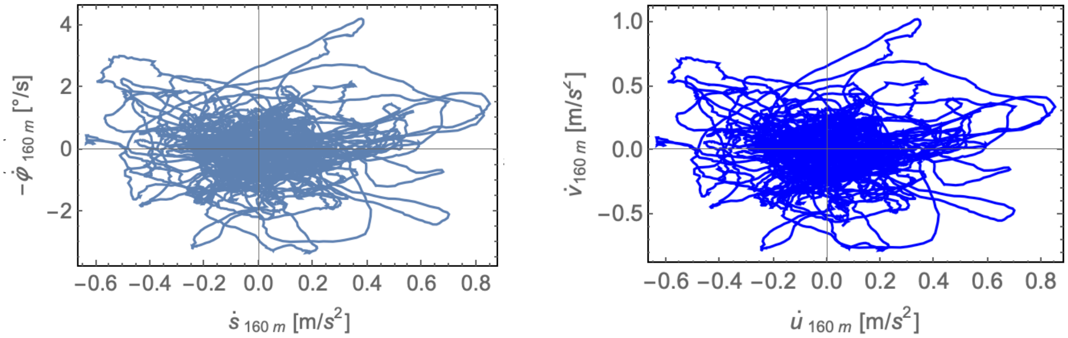

Figure 22. Acceleration space for a typical event at 160 m height; accelerations in terms of speed and negative direction (left), and in terms of $\dot{v}$ versus $\dot{u}$ (right).

From Figure 22we can also see that $\dot{v}$ versus $\dot{u}$ is nearly identical to $-\dot{\varphi}$ vs. $\dot{s}$. We also remind that both positive and negative values of $\dot{v}$ (or $\dot{\varphi}$) will affect a turbine, whereas mostly positive values of streamwise acceleration have an impact on loads. In the more typical event such as shown above, the accelerations $\dot{s}$ may be small enough such that the s does not cross V_{rated}, if the mean speed S differs significantly from V_{rated}.

3.4. Parameters for simulation with aeroelastic models

When identifying timeseries of extreme events, if these are to be used in constrained flow simulations with Mann-model turbulence as the basis (background), then the Mann-model parameters must be found which correspond to the flow during each event. The Mann turbulence model (Mann, 1994) has three parameters: the turbulence length scale L_{MM}, the inertial-range amplitude $\alpha\epsilon^{2/3}$, and the anisotropy or ‘eddy lifetime’ parameter Γ. As the Mann model is based on a three-dimensional spectral formulation, these parameters are directly obtainable by fitting to spectra of the three components of velocity in addition to the cross-spectrum of streamwise and vertical velocity. Although the IEC 61400-1 gives a crude prescription for site-specific Mann-model parameters based on mean wind speed and height, in both research and practice it is found that these differ from the parameters obtained from three-dimensional sonic anemometers. However, the relative rarity of 3d sonic anemometer use in industry, along with lacking a method to obtain $\{L_{\text{MM}}, \alpha\epsilon^{-2/3}, \Gamma\}$ from cup anemometers, means that at least for site assessment the oversimplified IEC prescription is commonly employed.

3.4.1. New method: Mann-model parameters from speed & direction data

Due to having access to only speed and direction data from 100 m and 160 m anemometers for much of the observational period (after 2014)—without three-dimensional velocity component data—and also because this is a common situation in wind energy, due to the prevalence of cup anemometers and wind vanes, it was necessary to create a method to practically derive the three Mann-model turbulence parameters from such typical measurements.

Kelly (2018) found that the Mann-model turbulence length scale was related to the shear by the simple form $L_{\mathrm{MM}} \simeq \sigma_u \cdot (\Delta U/\Delta z)^{-1}$. However, in the current application we are wanting to use timeseries from two different heights in constrained turbulence simulations, and must consequently deal with (at least implicitly) the vertical inhomogeneity; thus, we must find another way to get L_{MM} at each (single) height. Based on limited 3d measurements at 100 m and 160 m, and independent measurements from the other mast at 80 m height, the spectral tensor was calculated for the collection of extreme acceleration events identified (top 10 per wind speed bin for both streamwise and lateral, at each location). From the spectral tensor fits were made to obtain the three Mann-model parameters. To find the representative parameters including each event as well as the background turbulence, this was done twice: once on the 20 Hz data, and once on *spatially high-pass filtered* data using a filter scale of 2 km. The extreme events exhibited significant non-stationarity due to mesoscale (low-wavenumber) variance, so the background turbulence 'behind' each event was identified from fits to the spatially filtered data, while the turbulence including the large-scale signature of the event was obtained from the spectral fits to the unfiltered data. From these it was found that the turbulence length scale could be estimated most simply by using the integral time scale of lateral velocity fluctuations (integral length scale, via Taylor's hypothesis): the 'full' event-including turbulence with its non-stationarity had $L_{\mathrm{MM}} \approx 0.5 L_v \approx 0.5 T_v S$, while the background turbulence had $L_{\mathrm{MM,hp}} \approx 0.8 T_{v,\mathrm{hp}} S$, where the integral time scale is obtained by temporal autocorrelation and the subscript 'hp' denotes the background (spatially high-pass filtered) turbulence. These are shown in Figure 23 below.

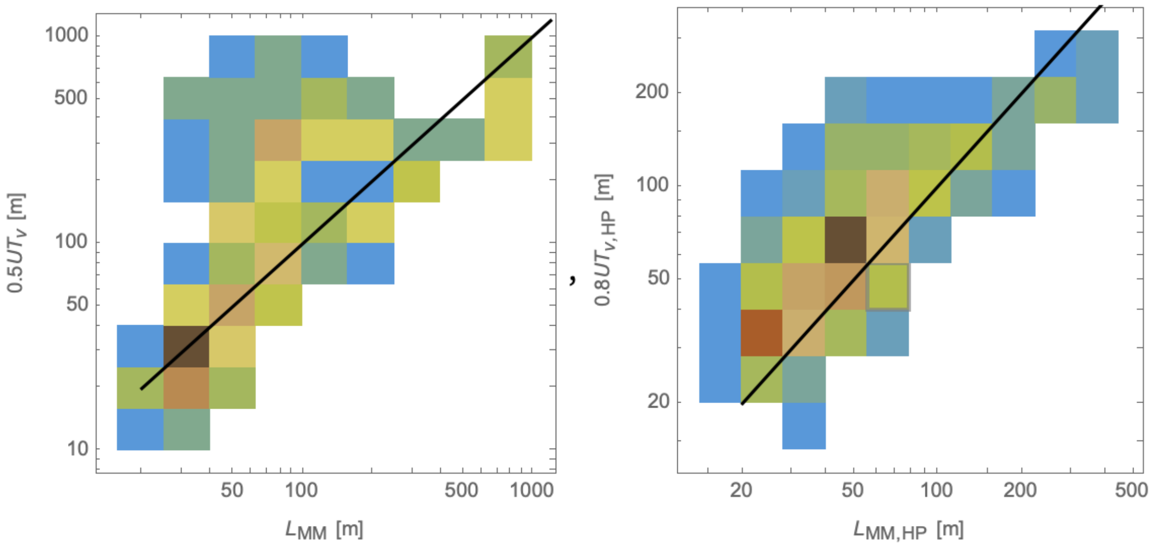

Figure 23. Estimates versus spectrally fit values of Mann-model length scale. Left: for raw timeseries of extreme events identified; right: for background turbulence, spatially high-pass filtered with f_c =S/2km.

To obtain the Mann-model inertial amplitude parameter, it was again found that the integral length scale of turbulent fluctuations served as a useful predictor. However, for $\alpha\epsilon^{2/3}$ the streamwise scale gave better predictions, in combination with the streamwise velocity variance; this is shown in Figure 24.

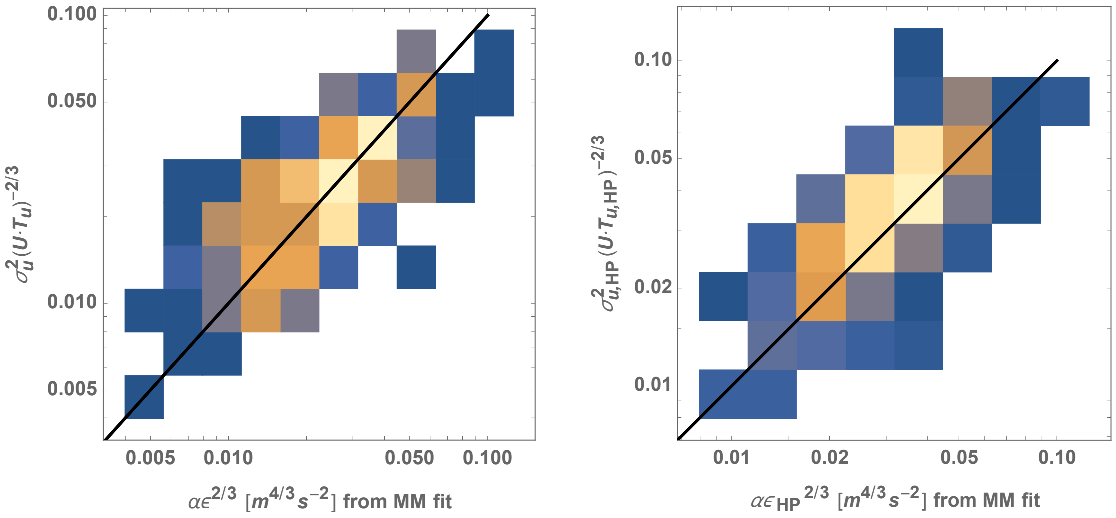

Figure 24.Estimates versus spectrally fit values of Mann-model amplitude parameter. Left: for raw timeseries of extreme events identified; right: for background turbulence, spatially high-pass filtered with f_c=S/2km.

As indicated by the solid lines in Figure 24, the spectral amplitude parameter for the full event timeseries was estimated as $\alpha\epsilon^{2/3} \approx \sigma_u^2(T_u S)^{-2/3}$; for the background (spatially high-pass filtered) turbulence the same form ensued, but with the corresponding variance $\sigma_{u,\mathrm{hp}}^2$ and integral time scale $T_{u,\mathrm{hp}}$.

Lastly, the anisotropy parameter Γ was found for background and full turbulence under all the extreme events; this is shown in Figure 25.

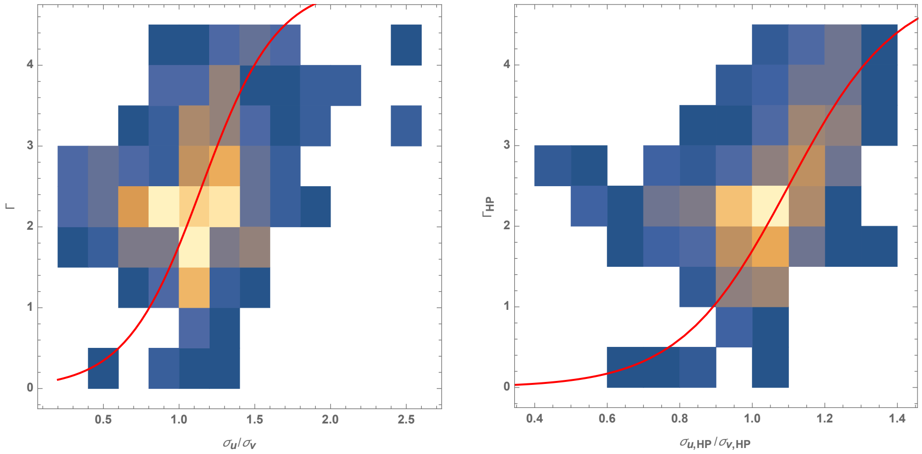

Figure 25. Mann-model anisotropy parameter: fitted values from spectral tensor versus σ_u/σ_v . Left: for raw timeseries of extreme events identified; right: for background turbulence, spatially high-pass filtered with f_c=S/2km.

The Γ-parameter was found to be described by $\Gamma \approx 2.5\left[1 + \tanh\left(\frac{\sigma_u/\sigma_v - 1}{0.3}\right)\right]$; this is shown by the red line in the figure above. The hyperbolic tangent (tanh) form is chosen because it limits the Γ-parameter to stay between 0 and 5, consistent with Mann (1994), and also accounts for some of the relatively large and small values of σ_u/σ_v encountered when analyzing more than just the extreme events (not shown). One can see appreciable apparent scatter compared to the parameterization, but we note that loads are insensitive to the value of Γ, as shown e.g. by the Sobol indices reported in Dimitrov *et al.* (2018).

From the full set of extreme events found at 100 m and 160 m, the parameterizations given above were used to find the Mann-model parameters for constrained turbulence simulations, which were shared with Hiperwind along with the event timeseries themselves.

4. Joint models for multivariate wind and wave conditions

Data for several wind and wave variables, from measurements near an operational wind farm, have been made available for constructing a joint distribution of wind and wave conditions. The data contain continuous measurements over a period of four years, from 2015 to 2018. A number of variables have been available, and this study has considered the following:

- Wind direction (θ) – ∈ (0°, 360°). Note the change in coordinate system compared with section 3: here in section 4, 0° corresponds to wind coming from the East and proceeds counter-clockwise with increasing θ (typical mathematical coordinates); previously (section 3) we had $\varphi = 0°$ denoting northerly winds, proceeding clockwise ('compass' coordinate system) for increasing φ.
- Mean wind speed (U) – 10-min. average horizontal wind speed at 10 m above sea level
- Turbulence (σ_s) – 10-minute standard deviation of wind speed
- Significant wave hight (H_s) – Significant wave height per 30 min., up-sampled to 10-min. values
- Wave direction (α) in degrees
    - Wind-wave misalignment (β) is difference between wind & wave directions: $\beta \equiv \theta - \alpha$
- Peak wave period (T_P) – Peak 1-hour spectral wave period, up-sampled to 10-min. values.

The data are collected at an ocean area just outside the wind farm, which is ~1–2 km from a coastline in a small range of directions; but due to the shape of the land nearby, for θ in a range of –30° (330°) to 120° (ENE to SSW) the environment can be considered as open sea. Hence, a different wind-wave climate is expected for different wind directions due to limited fetch from certain directions. We will focus on the open-sea conditions.

Pairwise scatter plots of the wind-wave data are shown in Figure 26 (anonymously, to protect proprietary information); rather than wave direction, the misalignment between wind and wave directions are shown. One particular feature of the data, which is clearly seen in scatter plots of significant wave height, is the occurrence of a few very large H_s values that stand out from the overall scatter. A few values of H_s occur above 18 m, whereas the bulk of the data hardly exceeds around 6 m.

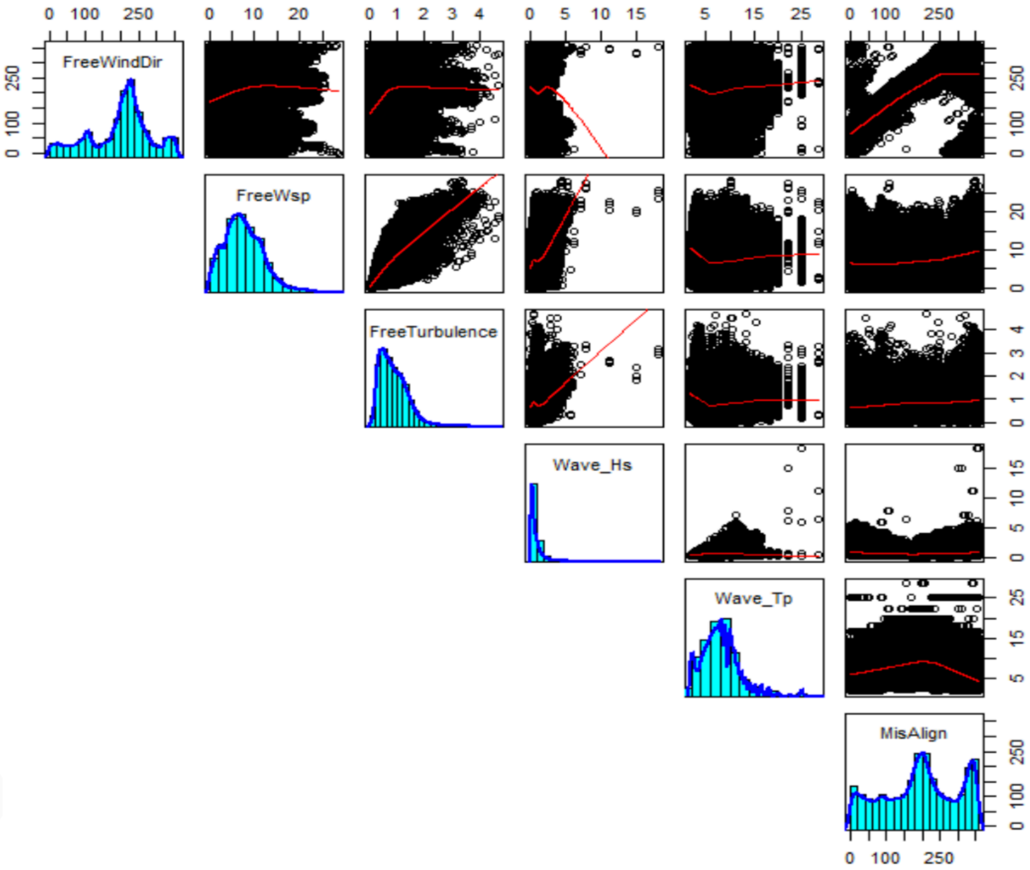

Figure 26. Marginal distributions and pairwise scatter-plots of wind-wave data from a coastal offshore site, considering all directions.

It turns out that all of the extreme values with $H_s > 6$ m are from one and the same period of time, i.e., from one particular storm. This can be seen from the time-series plots in Figure 27.

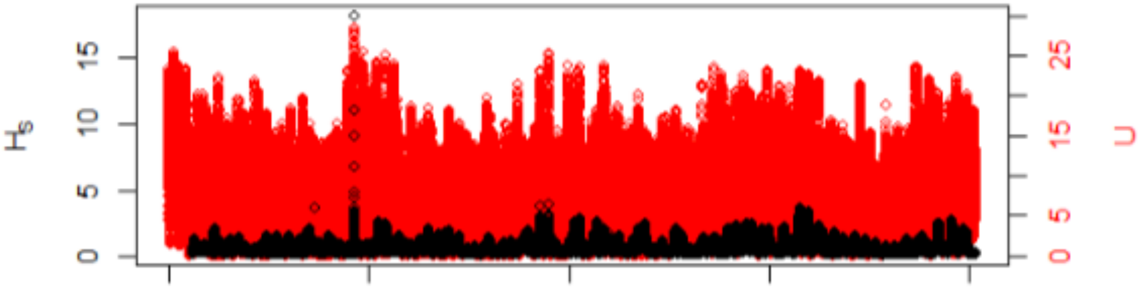

Figure 27. Significant wave height (black) and wind speed (red) over measurement period. Horizontal axis is time.

Similar features are not observed for the wind-variables, and this feature of the wave-data makes it particularly challenging to fit good statistical models to the wind-wave data. Moreover, zooming in on the time-series plot in Figure 27 reveals another feature of the wave data: due to the up-sampling of the wave data to ten-minute resolution, values of H_s appear in triplets of identical values. It is assumed that this particular feature in the data does not influence the fitted models much, but fitting good conditional models for the wave parameters remains challenging.

We note that the particular storm that resulted in the extreme significant wave height values had a wind direction θ between 330 and 360 degrees (i.e. from the southeast) and small misalignment; this can be seen in Figure 28. The figure further demonstrates how the shore-affected climate (150°–180° sector plots) varies significantly from the open sea wind-wave statistics; e.g. one can see the wind-wave misalignment for the near-shore (1–2 km fetch) sector is mostly far from 0° with shore-reflected waves often opposing wind (β from 90° to 270°), whereas for open ocean (330°–360° plots) the waves are not opposing the wind.

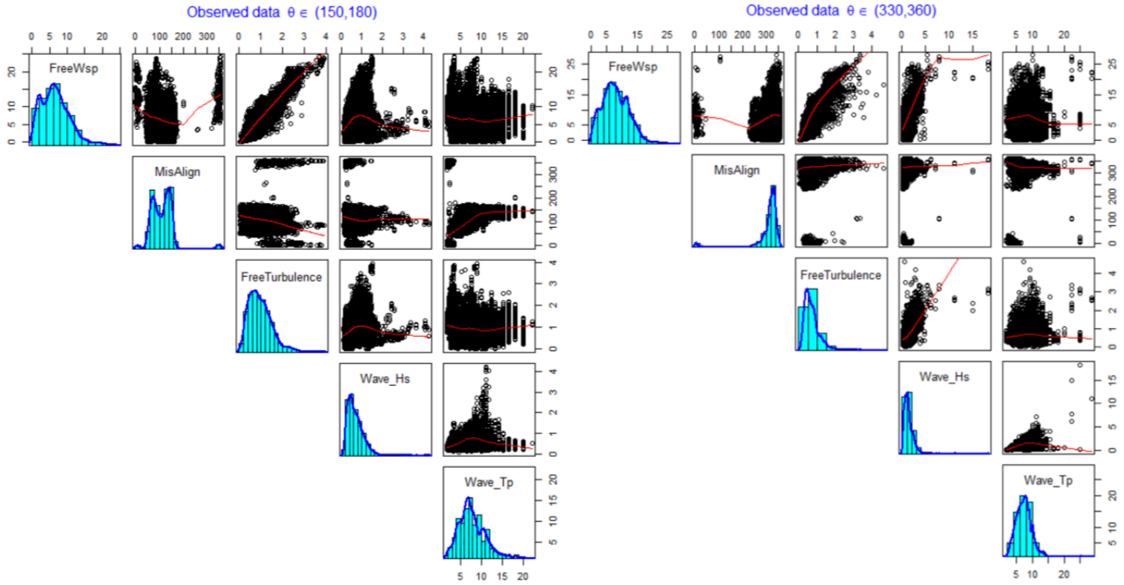

Figure 28. Marginal distributions and pairwise scatter-plots of wind-wave data from a coastal offshore site, over 4 years. Left: data from coastal low-fetch sector (θ from 150° to 180°); right: data from open ocean sector (θ from 330° to 360°).

Finally, it is also observed that even though the extreme values of H_s occur in a period where there is also extreme wind speeds, wind and wave extremes are not fully concurrent. There is a small time-lag between the highest wind speeds and the highest wave heights, and this delay contributes to making it difficult to fit good conditional models for the wave parameters conditioned on the concurrent wind speed. Notwithstanding, a joint distribution model for the simultaneous occurrence of wind and wave conditions will be fitted to these data.

4.1. Joint distribution modelling

In this study, multivariate joint distribution models are constructed, for selected sectors of wind direction, as a product of a marginal model for wind speed and a set of conditional models for the other variables. In particular, a simplified model is assumed, where conditional independence has been assumed for most other variables. In particular: turbulence, significant wave height and wind-wave misalignment is modelled conditional on wind speed; meanwhile, spectral peak wave period is modelled conditional on significant wave height. The different conditional models are assumed conditionally independent of the other variables. Hence, the joint model takes the following form:

$$f_{U,\sigma_u,H_s,T_p,\beta}\left(U,\sigma_u,H_s,T_p,\beta\right) = f_U(U) f_{\sigma_u|U}(\sigma_u|U) f_{H_s|U}(H_s|U) f_{T_p|H_s}(T_P|H_s) f_{\beta|U}(\beta|U) \qquad (2)$$

Different models are explored for the different marginal and conditional models, and the selected models are outlined in the following.

For the marginal distribution of wind speed, a hybrid model consisting of a Weibull distribution for the body and a generalized Pareto distribution (GPD) for the tails is assumed. The cumulative distribution function for wind speed is hence as follows:

$$F_U(u) = \begin{cases} F_W(u) & {\scriptstyle 0\le u\le v} \\ F_W(v) + [1 - F_W(v)]G(u) & {\scriptstyle u>v} \end{cases} \tag{3}$$

where $F_W(u)$ is the Weibull cumulative distribution function,

$$F_W(u) = 1 - \exp[-(u/A_w)^{k_W}] \quad \text{for } u>0 \tag{4}$$

and $G(u)$ is the generalized Pareto cumulative distribution function

$$G(u) = \begin{cases} 1 - \left[1 + \frac{\xi(u-v)}{\sigma_G}\right]^{-1/\xi} & \text{for } \xi \neq 0 \\ 1 - \exp\left(\frac{u-v}{\sigma_G}\right) & \text{for } \xi = 0 \end{cases} \tag{5}$$

with support on $u \geq v$ for $\xi \geq 0$ and on $u \leq (v - \sigma_G/\xi)$ when $\xi < 0$. That is, with a finite upper bound for negative GPD shape parameter ξ. Thus has the following parameters that are fitted from the data by maximum likelihood: Weibull shape k_W, Weibull scale A_W, threshold v, GPD shape ξ and tail fraction ϕ corresponding to the probability of being above the threshold v. In addition, the GPD scale parameter σ_G can be estimated from the data, or by imposing a continuity constraint on the distribution function it will be estimated from the other parameters. Alternatively, 3-parameter translated Weibull distributions are also fitted to the wind speed data, for two different fitting methods, and compared to the hybrid Weibull-GPD models. The fitting methods for the Weibull distributions are maximum likelihood and minimization of the second order Anderson-Darling statistic. Both distributions yield reasonable fits to the data, and the hybrid model is selected in the following.

The conditional probability density function of turbulence (10-minute standard deviation of streamwise wind fluctuations) conditioned on mean wind speed is modelled as a log-normal distribution,

$$f_{\sigma_u|U}(\sigma|u) = \frac{1}{\tau_\sigma(u)\sigma\sqrt{2\pi}} \exp\left[-\frac{\left(\ln\sigma - \mu_\sigma(u)\right)^2}{2\left(\tau_\sigma(u)\right)^2}\right], \tag{6}$$

where the model parameters μ_σ and τ_σ are modelled as a function of wind speed assuming a power-law relationship:

$$\mu_\sigma(u) \equiv \text{mean}[\ln\sigma_u \,|(U=u)] = \; a_1 + b_1 u^{c_1}$$

$$\tau_\sigma(u) \equiv \text{std. dev.}\,[\ln\sigma_u \,|(U=u)] = \; a_2 + b_2 u^{c_2}.$$

The conditional distribution of turbulence given wind speed is specified by the six parameters a_1, b_1, c_1, a_2, b_2 and c_2. These are estimated from the data by collecting data in bins of 2 m/s wind speed and calculating the expected value and standard deviation of $\ln\sigma_u$ in each bin, and then fitting the dependence by nonlinear least squares.

For the conditional distribution of significant wave height, given wind speed, a 3-parameter translated Weibull distribution is assumed. That is, the density function for H_s is given by

$$f_{H_s|U}(h|u) = \frac{k_{W,h}(u)}{A_{W,h}(u)}\left(\frac{h-\gamma_{W,h}(u)}{A_{W,h}(u)}\right)^{k_{W,h}(u)-1} \exp\left[-\left(\frac{h-\gamma_{W,h}(u)}{A_{W,h}(u)}\right)^{k_{W,h}(u)}\right] \tag{7}$$

where the Weibull-parameters for the conditional H_s distribution are denoted by $\{A_{W,h}, k_{W,h}, \gamma_{W,h}\}$, to distinguish them from the two Weibull parameters in the wind-distribution of (4).

Again, different parametric functions were used to try to capture the dependence of model parameters on wind speed, including a power-law fit and a polynomial fit. However, for some sectors of wind speed, it would be difficult to fit a power-law function and the polynomial fit, although fitting the data quite well, could yield unreasonable results when extrapolating (e.g., negative shape and scale parameters). Therefore, piecewise constant 3-parameter Weibull distributions were assumed within each 2 m/s bin of wind speed. Hence, to fully specify this model, the three Weibull parameters need to be estimated within each bin, resulting in $3 \times N_u$ parameters, where N_u represents number of wind speed bins. For example, with 13 bins of wind speed, 39 parameters are needed to specify this model. Alternatively, results for a 3-parameter translated Weibull distribution, where a power-fit for the relationship between model parameters and wind speed are assumed and where the model parameters are assumed constant if a power-law fit is not successful, were also obtained. As a second alternative, a conditional log-normal model for significant wave height, where the relationship between the model parameters and wind speed is fitted by a power-law model for the location parameter, and either an exponential fit or a 3rd-order polynomial fit for the scale parameter, was tried. Due to the challenge of fitting good conditional models for H_s given U, all these alternatives are fitted, possibly with a preference for the piecewise constant Weibull distribution. The power-law relationship is similar to the models used for turbulence, and the exponential and polynomial models are respectively

$$p_W(u) = a_3 + b_3 e^{c_3 u} \quad \text{or} \qquad p_W(u) = a_3 + b_3 u + c_3 u^2 + d_3 u^3$$

where p_W can be any of $\{A_{W,h}, k_{W,h}, \gamma_{W,h}\}$.

The conditional distribution of spectral peak period given significant wave height, i.e., $f_{T_p|H_s}$, is assumed to be a lognormal distribution with PDF having the form of (6). Again, the relationship between the model parameters and significant wave height are modelled by a parametric function, based in this case on H_s bins of width 1 m. A power-law function is assumed for the location parameter, and an exponential relationship is assumed for the scale parameter, as suggested in the 2021 update of DNV's recommended practices (DNV, 2019), as follows:

$$\mu_{T_p}(h) \equiv \text{mean}\left[\ln T_p \,\middle|(H_s = h)\right] = \; a_4 + b_4 u^{c_4}$$

$$\tau_{T_p}(h) \equiv \text{std. dev.}\left[\ln T_p \,\middle|(H_s = h)\right] = \; a_5 + b_5 u^{c_5}.$$

Hence, this model is fully specified by the six parameters $\{a_4, b_4, c_4, a_5, b_5, c_5\}$, and these are fitted to the data by calculating their values in 1 m bins of H_s and then fitting the functional relationship by nonlinear least squares. It is noted that two alternative fits of this model is obtained, where the alternative fit only uses points for H_s bins with at least 10 observations, and additional constraints are put on the τ_{T_p} parameter for lower H_s values.

Finally, the conditional distribution of wind-wave misalignment β, if considering all directions, is modelled by a mixture of two von Mises distributions. The von Mises distribution is a distribution for cyclic variables. The PDF of a von Mises mixture with *n* components has the following form:

$$f_\beta(\beta) = \sum_{i=1}^{n} \omega_i \, f_i(\beta) \qquad (8)$$

with $0 \leq \omega_i \leq 1$ and $\sum_{i=1}^{n} \omega_i = 1$, where the von Mises form itself is

$$f_i(\beta) = \frac{\exp[\kappa_i \cos(\beta - \delta_i]}{2\pi I_0(\kappa_i)} \, . \qquad (9)$$

Here $I_0(\kappa)$ is the modified Bessel function of the first kind, of order 0, with concentration factor κ. Hence, this distribution is specified by the three parameters: location δ, concentration κ and weight ω per mixture component. In this study, a mixture with *n* = 2 components is assumed. Moreover, a von Mises mixture is estimated within each bin of 2 m/s of wind speed, but in bins where the data do not support a mixture, a single von Mises distribution is used. Since it is not reasonable to interpolate the parameters of the von Mises mixtures, piecewise constant models are assumed within each bin rather than to fit a parametric function for the dependence. In the case of only open-ocean directions, then only a single component is used, and the simple PDF (9) represents the misalignment probabilities.

The parametric multivariate distribution model described by (2)–(9) is fitted to the wind-wave data for selected sectors of wind direction, as outlined in the following subsections.

4.1.1. Fitted joint models

Having established the framework for the joint distribution models and specified the marginal and conditional models for all the variables, this model is fitted to the wind-wave data. First, a crude model is fitted to the omnidirectional data. Then, similar models are fitted to specific sectors of wind direction of particular interest.

4.1.1.1. Omnidirectional fits

The following results indicate the joint models fitted to the omnidirectional data for all wind directions, i.e. including a mix of open-sea and limited-fetch coastal conditions. The fitted marginal distribution for wind speed, *U* is illustrated in Figure 29, and it is observed that the hybrid Weibull-GPD distribution with continuity constraints on the density fits reasonably well.

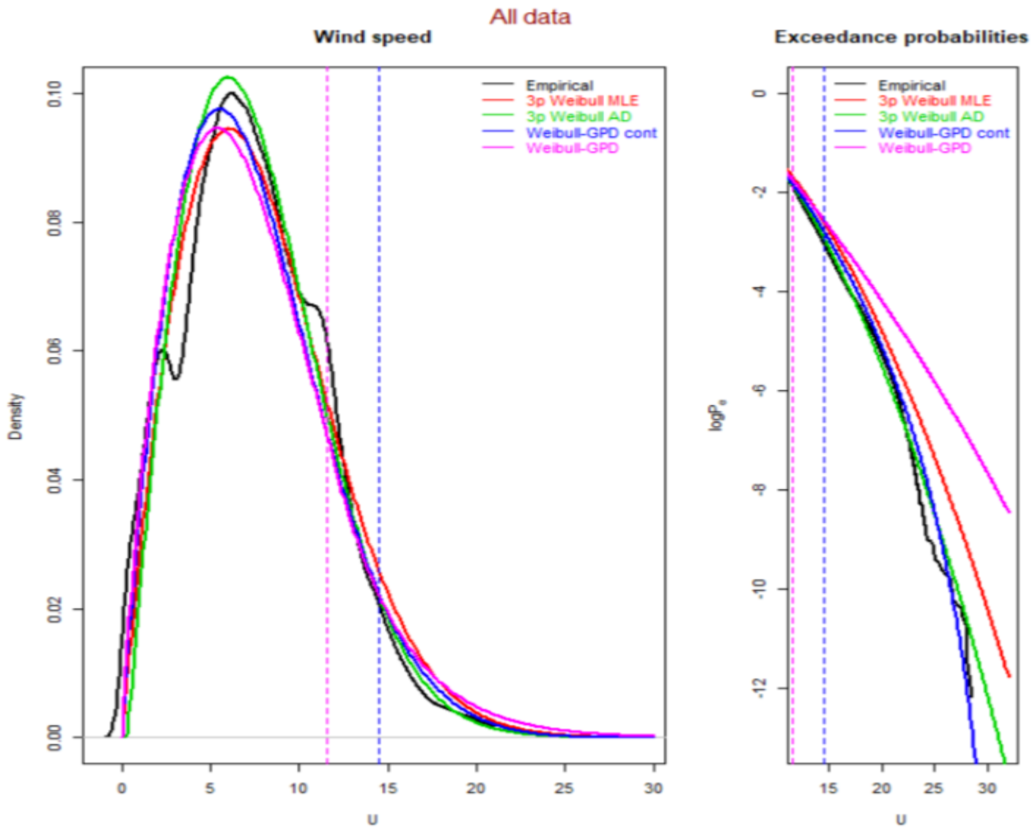

Figure 29. Fitted marginal distribution for omnidirectional wind speed data.

The fitted conditional model for turbulence given wind speed, are illustrated by the fitted relationships in Figure 30 below. The μ_σ and τ_σ are calculated using 2 m/s bins of wind speed, and the power-law fit is found to fit these data reasonably well.

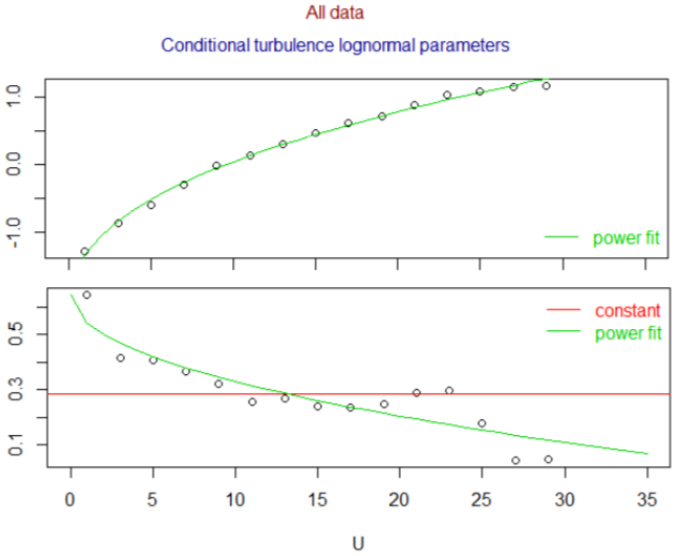

Figure 30. Fitted conditional model for turbulence standard deviation, given wind speed. Top: $\mu_\sigma(U)$; bottom: $\tau_\sigma(U)$.

The conditional model for significant wave height given wind speed is challenging, and alternative fits are shown in Figure 31below. For the omnidirectional data, it appears that both the power-fit and the polynomial fit for the Weibull parameters work well. However, it is noted that extrapolation to higher wind speeds yields decreasing shape parameter and increasing scale parameters and might hence be expected to yield quite large values of significant wave height. Notwithstanding, the power-law fit to the Weibull parameters is found to work well for these data. Conditional log-normal parameters and fitted dependence models are also shown in Figure 31, but are not found to work very well.

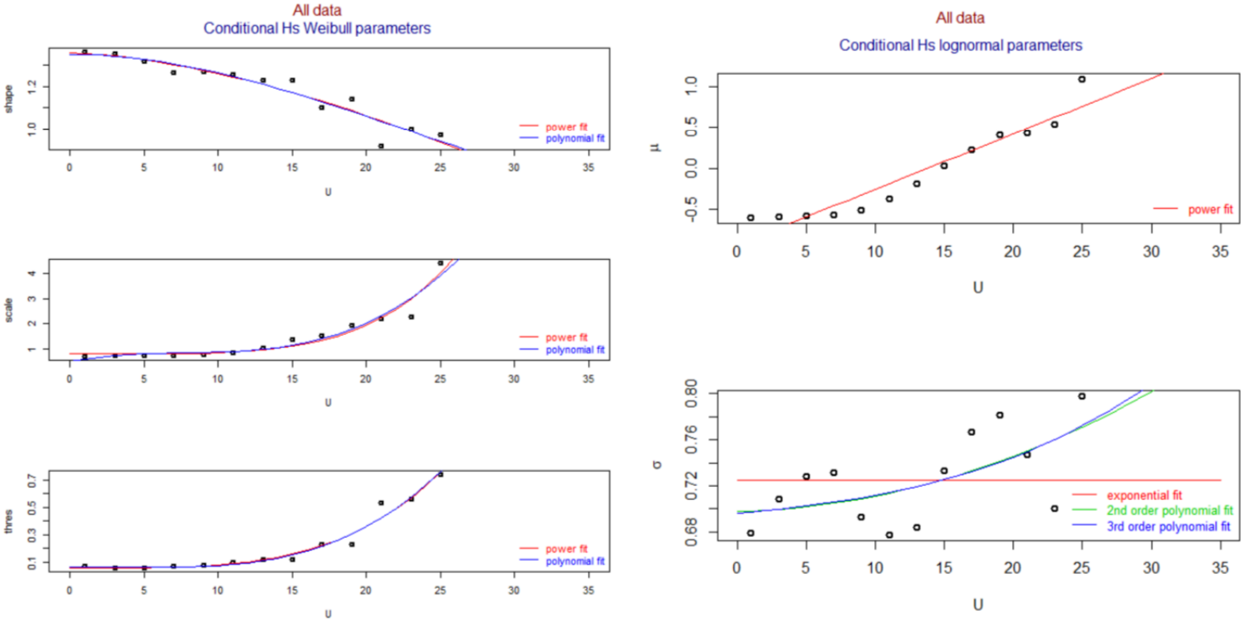

Figure 31. Fitted conditional model for omnidirectional significant wave height data per wind speed. Left: 3-parameter Weibull; right: lognormal distributions.

The conditional model for spectral peak wave period given significant wave height, i.e., $f_{T_p|H_s}$, is fitted based on calculating the model parameters in 1 m wide bins of H_s and fitting the dependence models. This is shown in Figure 32. The alternative fit is based on bins with at least ten observations, and with an additional upper constraint on the τ_{T_p} parameter.

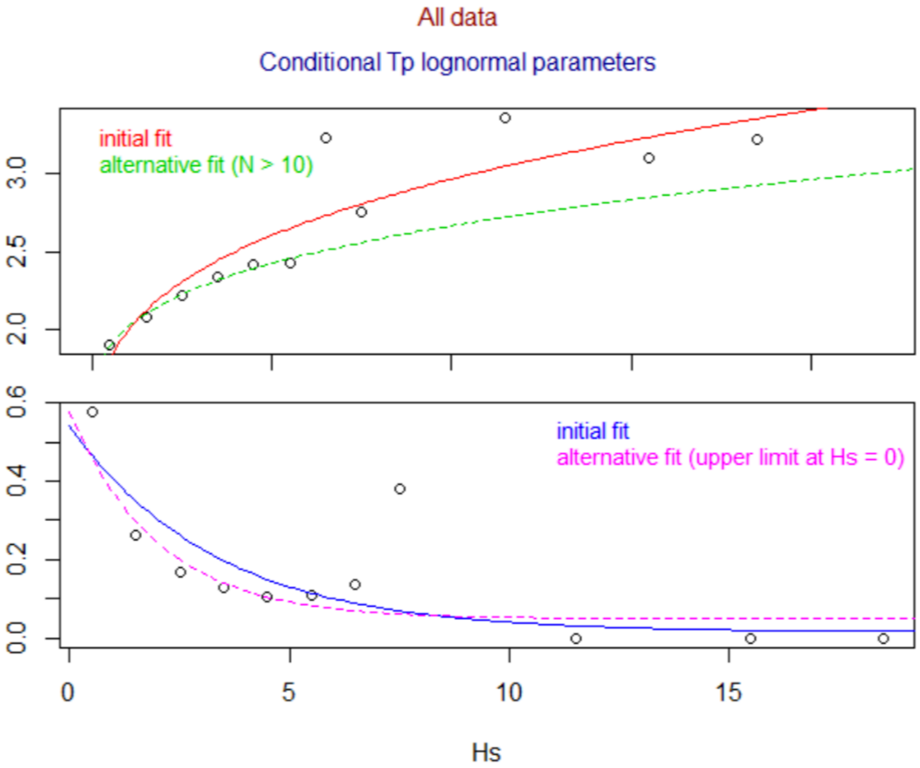

Figure 32. Fitted conditional model for omnidirectional wave period data given significant wave height.

Finally, the conditional model for wave-wind misalignment is assumed to be a piecewise constant mixture of two von Mises distributions within each 2 m/s bin of wind speed. The fitted models are illustrated in Figure 33, where the empirical densities within each wind speed bin are plotted together with a single von Mises distribution and a mixture of von Mises distributions, respectively. Note that for some of the bins, there were not support in the data to fit a mixture, and a single von Mises distribution was assumed.

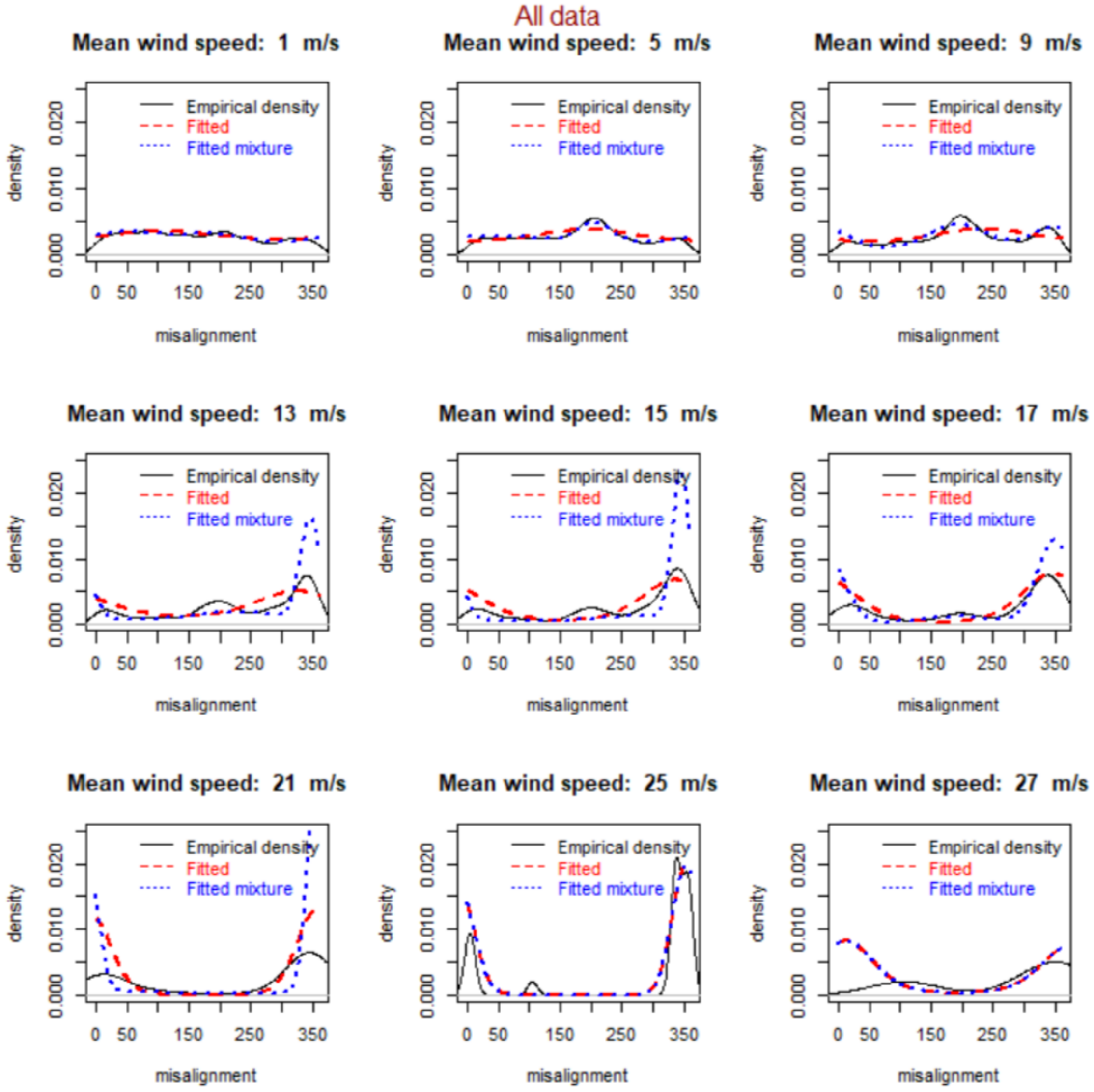

Figure 33. Fitted conditional models for omnidirectional wind-wave misalignment data, given wind speed, for selected bins.

4.1.1.2. Joint models for open sea conditions

It is acknowledged that the wind-wave climate will be affected by the presence of the coastline to the west of the observed ocean area, and that using data for the open sea wind directions should give different—and more universally applicable—results. Hence, the same parametric model is fitted to data with wind directions $\theta \in [330°, 120°]$. Results from fitting the marginal model and the various conditional models to these data are shown in Figure 34 and Figure 35 below.

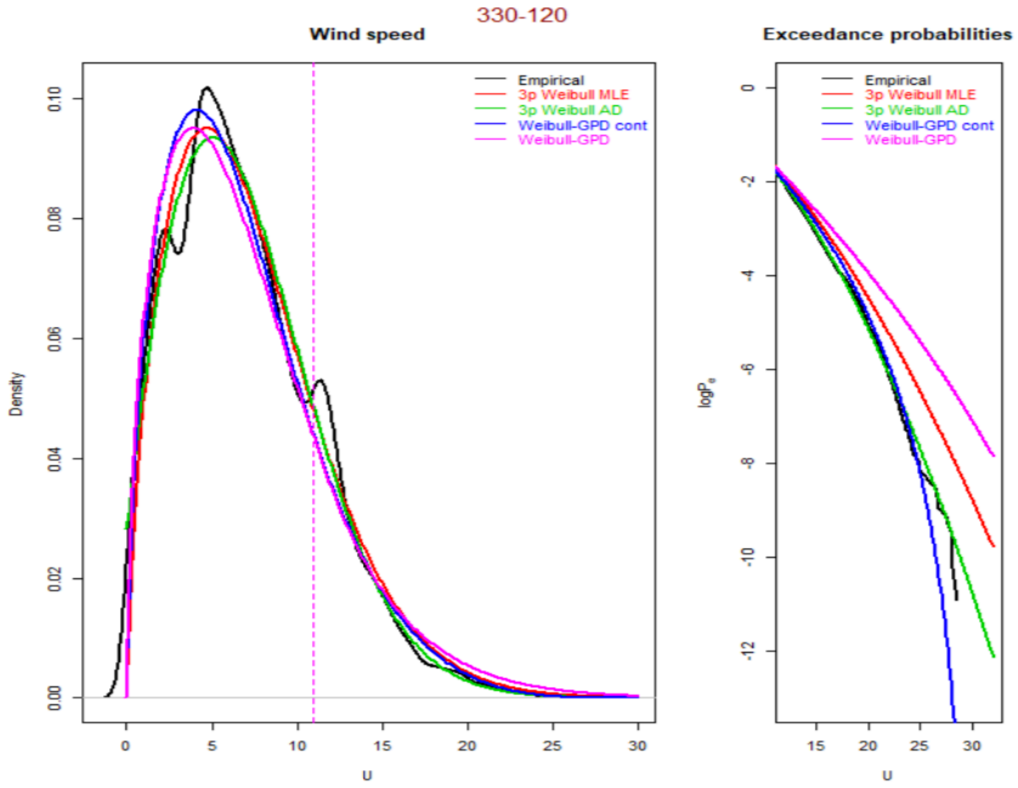

Figure 34. Fitted marginal distributions for open sea wind direction data.

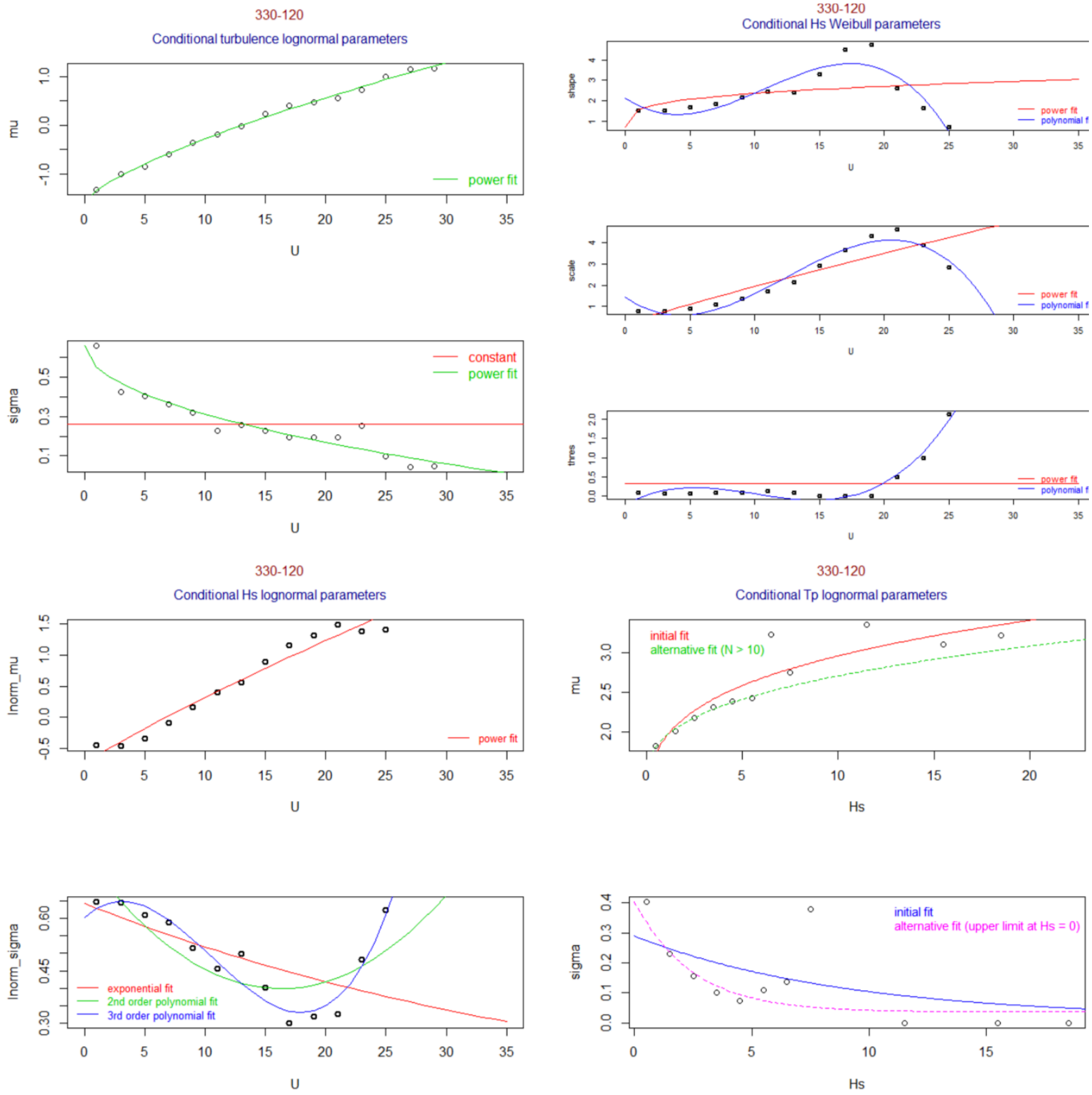

Figure 35. Fitted conditional distributions for open sea wind direction data. Note "lnorm_sigma" refers to τ-parameter.

Simulated data from the fitted models, where four different alternatives for the conditional PDF $f_{H_s|U}(h|u)$ are tried out, are shown in Figure 36. All model alternatives look somewhat reasonable, but possibly with a preference for the piecewise-constant Weibull distribution for significant wave height H_s.

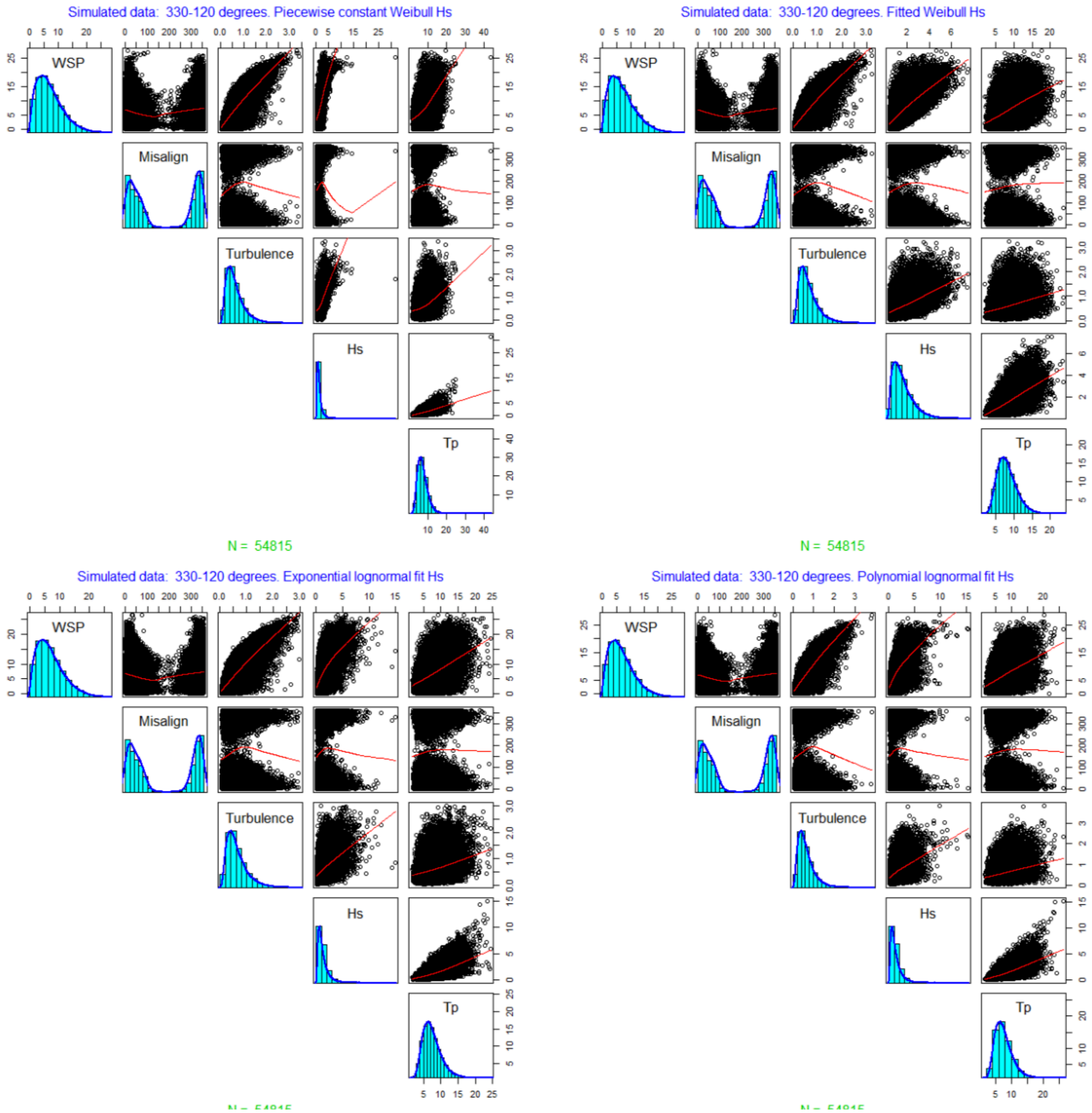

Simulated data: 330-120 degrees. Piecewise constant Weibull Hs

Simulated data: 330-120 degrees. Fitted Weibull Hs

Simulated data: 330-120 degrees. Exponential lognormal fit Hs

Simulated data: 330-120 degrees. Polynomial lognormal fit Hs

Figure 36. Simulated data from the fitted model; open-sea directions only.

To get an idea how this model extrapolates, simulated datasets of 40 and 400 years respectively (10 and 100 times as much data as in the four-year dataset used for model fitting), are shown in Figure 37. The number of simulated samples are indicated in the plots.

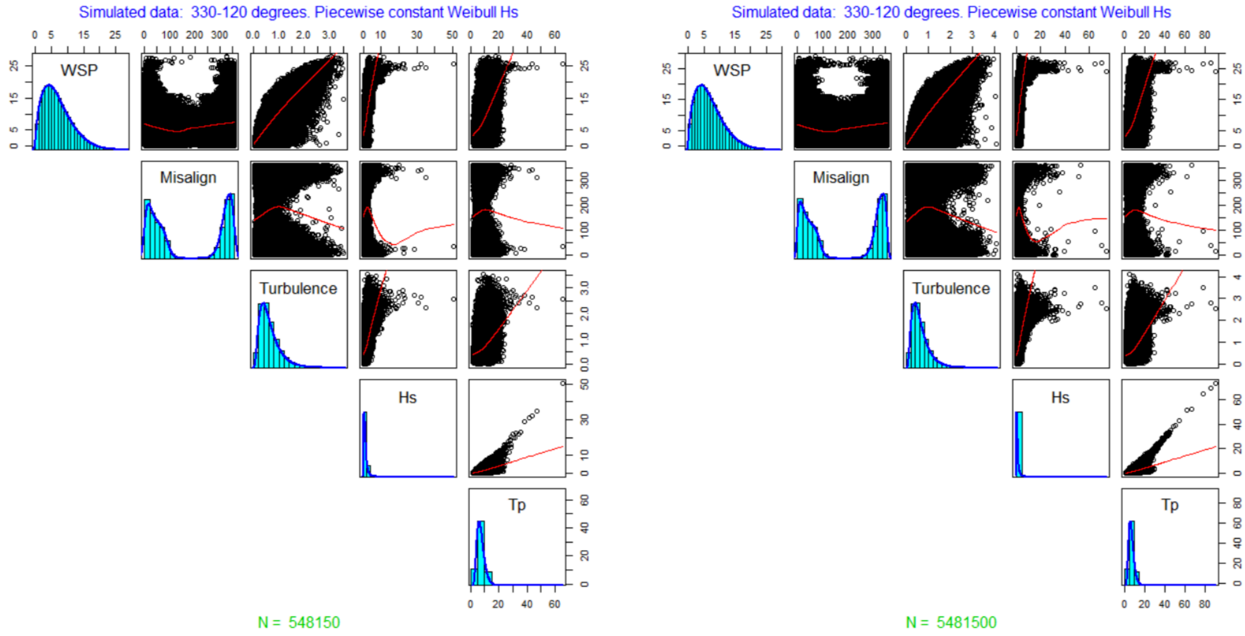

Figure 37. Extended simulated data from the fitted model, for open-sea directions. Left: 40 years of simulation; right: 400 y.

Fits like the above, but per 30° sector were also made. These will be provided to the project partners as well, along with uncertainty estimates for the parameters.

5. Conclusions

A number of useful innovations and findings were made in WP2, as reported above, which also led to results (derived data and parameters for simulations) shared with the partners to use in WP3 and WP4. In short we found some universal behavior of the largest accelerations occurring in 10-minute periods, which can be adjusted (filtered) according to characteristic turbine response time. These can be exploited to get load-driving acceleration maxima, both for fatigue loads and also N-year extreme estimates; the latter were also derived and given above. It was fundamentally confirmed that the statistics of common fatigue-inducing streamwise accelerations can be captured using 10-minute averages, as in the IEC standard; simple relations for the 10-minute 99th percentile of streamwise acceleration ($\dot{s}_{99}$ or $\dot{u}_{99}$) were given in terms of 10-minute standard deviation of wind speed σ_s, and also conditioned on wind speed itself. However, extreme $\dot{s}_{99}$ cannot be captured by 10-minute statistics, and were found to not track with mean wind speed. The extreme events were often associated with shallow atmospheric boundary layer conditions, but arise due to a number of different physical mechanisms. A good fraction (majority) of them also involved wind speed crossing typical rated speeds for modern turbines. Lateral acceleration events ($\dot{\varphi}_{99}$ or $\dot{v}_{99}$) were also detected and found to be independent of mean wind speed. Extreme lateral-acceleration events occurred mostly at different times than the streamwise events, though a small fraction of events were both lateral and streamwise. For constrained turbulence simulation of load-inducing events, a new method to estimate Mann-model parameters from typical measurements was created; having tested this method, it was then applied to find the parameters corresponding to both the background turbulence and event-affected timeseries for the 360 most extreme events (10 strongest events in each of lateral and streamwise type, at both heights of 100 m and 160 m, per 9 wind speed bins of 1m/s width ranging from 8–17m/s).

Future and ongoing work includes treatment of the deviation of extreme $\dot{s}_{99}$ from a log-normal distribution (e.g, following a GEV or Gumbel-like form), deeper investigation of wind-speed dependence over a wider range, and identification of specific driving mechanisms for the events through comparison with more meteorological and mesoscale model data.

Joint-PDF models were also adapted and applied to wind-wave data at a commercial site using four years of mast and buoy data, with reasonable fits allowing synthesis of data for longer time periods. Ongoing work includes uncertainty quantification of the parameters within the joint-PDF modelling, and providing the environmental contours found from the analysis here to WP3-4.

6. References

N.K. Dimitrov, M. Kelly, A. Vignaroli, and J. Berg (2018): “From wind to loads: wind turbine site-specific load estimation with surrogate models trained on high-fidelity load databases”, *Wind Energ. Sci.* **3**(2), 767–790, https://doi.org/10.5194/wes-3-767-2018.

Á. Hannesdóttir, M. Kelly, and N.K. Dimitrov (2017): “Extreme variance vs. turbulence: What can the IEC cover?” *Wind Energy Denmark 2017* (poster session), Herning, Denmark.

Á. Hannesdóttir, M. Kelly, and N.K. Dimitrov (2019): “Extreme fluctuations of wind speed for a coastal/offshore climate: statistics and impact on wind turbine loads”, *Wind Energ. Sci.* **4** (2), 325–342, https://doi.org/10.5194/wes-4-325-2019.

International Electrotechnical Commission: *IEC 61400-1 Wind turbines—Part 1: Design requirements, 3rd ed.*, International Electrotechnical Commission, Geneva, Switzerland, 2005.

International Electrotechnical Commission: *IEC 61400-1 Wind turbines—Part 1: Design requirements, 4th ed.*, International Electrotechnical Commission, Geneva, Switzerland, 2019.

K.S. Hansen and G.C. Larsen (2007): “Full scale experimental analysis of extreme coherent gust with wind direction changes (ECD)”, *J.Phys.: Conf. Ser.* **75**, 012055.

M. Kelly (2018): “From standard wind measurements to spectral characterization: turbulence length scale and distribution”, *Wind Energ. Sci.*, **3** (2), 533–543, https://doi.org/10.5194/wes-3-533-2018.

M. Kelly, S.J. Andersen, and Á. Hannesdóttir (2021): “Statistical impact of wind-speed ramp events on turbines, via observations and coupled fluid-dynamic and aeroelastic simulations”, *Wind Energ. Sci.* **6**(5), 1227–1245, https://doi.org/10.5194/wes-6-1227-2021.

G.C. Larsen and K.S. Hansen (2008): “Rational Calibration of Four IEC 61400-1 Extreme External Conditions”, *Wind Energ.* **11** (6), 685–702, https://doi.org/10.1002/we.302.

S. Liu and X.-Z. Liang (2010): “Observed Diurnal Cycle Climatology of Planetary Boundary Layer Height”, *J. Climate* **23**, 5790–5809.

J. Mann (1994): “The spatial structure of neutral atmospheric surface-layer turbulence”, *J. Fluid Mech.* **273**, 141–168.

M. Nielsen, G.C. Larsen, J. Mann, S. Ott, K.S. Hansen, and B.J. Pedersen (2004): “Wind simulation for extreme and fatigue loads”. *Risø tech. rep.,* Risø-R-1437(EN), 104 pp.

Den Norske Veritas [DNV] (2021): “Environmental Conditions and Environmental Loads”, *DNV recommended practices report* DNV-RP-C205, Sept.2019 edition, 2021 update.

J.C. Wyngaard (2010): *Turbulence in the Atmosphere*, Cambridge Univ. Press, 393pp.

R.J. Yamartino (1984): “A comparison of several ‘single-pass’ estimators of the standard deviation of wind direction.” *J. Clim. & Appl. Meteorol.* **23**(9): 1362–1366.